Energy Transfer from High-Shear, Low-Frequency Internal Waves to High-Frequency Waves near Kaena Ridge, Hawaii

OLIVER M. SUN AND ROBERT PINKEL

Marine Physical Laboratory, Scripps Institution of Oceanography, La Jolla, California

ABSTRACT

Evidence is presented for the transfer of energy from low-frequency inertial–diurnal internal waves to high-frequency waves in the band between 6 cpd and the buoyancy frequency. This transfer links the most energetic waves in the spectrum, those receiving energy directly from the winds, barotropic tides, and parametric subharmonic instability, with those most directly involved in the breaking process. Transfer estimates are based on month-long records of ocean velocity and temperature obtained continuously over 80–800 m from the research platform (R/P) *Floating Instrument Platform* (*FLIP*) in the Hawaii Ocean Mixing Experiment (HOME) Nearfield (2002) and Farfield (2001) experiments, in Hawaiian waters. Triple correlations between low-frequency vertical shears and high-frequency Reynolds stresses, $\langle u_i w \partial U_i / \partial z \rangle$, are used to estimate energy transfers. These are supported by bispectral analysis, which show significant energy transfers to pairs of waves with nearly identical frequency. Wavenumber bispectra indicate that the vertical scales of the high-frequency waves are unequal, with one wave of comparable scale to that of the low-frequency parent and the other of much longer scale. The scales of the high-frequency waves contrast with the classical pictures of induced diffusion and elastic scattering interactions and violates the scale-separation assumption of eikonal models of interaction. The possibility that the observed waves are Doppler shifted from intrinsic frequencies near f or N is explored. Peak transfer rates in the Nearfield, an energetic tidal conversion site, are on the order of 2×10^{-7} W kg^{-1} and are of similar magnitude to estimates of turbulent dissipation that were made near the ridge during HOME. Transfer rates in the Farfield are found to be about half the Nearfield values.

1. Introduction

Internal wave energy and shear in the oceans are concentrated near the low-frequency, inertial end of the spectrum. Evidence for the direct breaking of these energetic low-frequency waves is limited. Klymak et al. (2008) have observed the convective instability of the semidiurnal baroclinic tide immediately above its generation site at Kaena Ridge, Hawaii. Alford and Gregg (2001) describe the dissipation of a low-latitude inertial wave by Kelvin–Helmholtz instability. In general, it is thought that energy is first transferred from low to higher-frequency internal waves and that these waves subsequently break (e.g., Alford and Pinkel 2000a,b).

Resonant interaction theory, beginning with Phillips (1960) and developed by Hasselmann (1962), Benney and Saffman (1966), McComas and Bretherton (1977), McComas and Müller (1981), Müller et al. (1986), and many others, predicts energy transfers between triads of internal waves with wave vectors ($\mathbf{k}_1$, $\mathbf{k}_2$, $\mathbf{k}_3$) and frequencies (ω_1, ω_2, ω_3), which together satisfy the resonance conditions

$$\mathbf{k}_1 + \mathbf{k}_2 + \mathbf{k}_3 = 0 \quad \text{and} \tag{1}$$

$$\omega_1 + \omega_2 + \omega_3 = 0. \tag{2}$$

Each wave also approximately satisfies the linear dispersion relationship

$$\omega^2 = \frac{f^2 m^2 + N^2(k^2 + l^2)}{k^2 + l^2 + m^2}, \quad \mathbf{k} = (k, l, m), \tag{3}$$

where N is the Brunt–Väisälä frequency and f is the inertial frequency.

Evaluations of energy transfer rates within a Garrett–Munk (GM) spectrum (Munk 1981) found that scale-separated interactions are likely to be important because of the wavenumber slope of the spectrum. Three limiting cases of scale separation were identified by McComas

Corresponding author address: Oliver M. Sun, Woods Hole Oceanographic Institution, M.S. 21, Woods Hole, MA 02543.
E-mail: osun@whoi.edu

and Bretherton (1977), who named the interactions induced diffusion (ID), elastic scattering (ES), and parametric subharmonic instability (PSI). ID involves an energy exchange between two high-frequency waves that have small spatial scales (large wavenumbers) and a third, much lower–frequency wave with large spatial scale (small wavenumber). Because the large wave vectors of the high-frequency waves differ by the small wave vector of the low-frequency wave, ID shifts wave action by a small distance in wavenumber space. In the limit of large-spatial-scale separation, wave action tends to be diffused in wavenumber space. ES also connects a low-frequency wave with a pair of high-frequency waves. The high-frequency waves have nearly opposite vertical wavenumber, with about half the wavelength of the low-frequency wave, and hence the process is reminiscent of Bragg scattering. The ES triad is not widely separated in vertical wavenumber, but the horizontal wavenumbers (and hence the frequencies) of the scattered waves may be large. In PSI, unlike the other two triads, energy is transferred between one wave and a pair of nearly half-frequency waves. These subharmonics have nearly opposite wave vectors (in both the horizontal and the vertical) and thus may have large vertical wavenumbers relative to the original.

Resonant interaction theory is exact only in the weakly nonlinear limit. Eikonal or ray-tracing methods have been also used to model interactions of small-scale test waves as they pass through and are refracted by a background field of large-scale waves (Henyey and Pomphrey 1983; Henyey et al. 1986; Broutman and Young 1986). This model allows stronger background fields than in the resonant theory, but it assumes, rather than demonstrates, a scale separation between the test waves and the background. [Henyey et al. (1986) find that the results remain qualitatively valid up to ''scale equivalence.''] Also, the test waves interact only with the background and not one another, so that the notion of a resonant triad is lost.

Measured open-ocean turbulence dissipation rates are reasonably consistent with the predictions of resonant interaction theory (Henyey et al. 1986; Gregg 1989; Polzin et al. 1995). However, direct observations of nonlinear energy transfer to high-frequency internal waves (e.g., statistically significant bicoherences showing phase coupling between triads of waves) are few. The slowness of the energy transfers in a ''typical,'' near-GM ocean has been viewed as a significant obstacle to achieving statistically significant observations over the length of a feasible field experiment (McComas and Briscoe 1980). A few studies have examined correlations between high-frequency wave stresses and low-frequency shears that are likely associated with near-inertial waves (Jacobs and Cox 1987; Duda and Jacobs 1998).

The present study documents nonlinear interactions between low- and high-frequency internal waves near Kaena Ridge, Hawaii, a site of intense barotropic-baroclinic conversion. We use data collected aboard the research platform (R/P) *Floating Instrument Platform* (*FLIP*) during 2001–02 as part of the Hawaii Ocean Mixing Experiment (HOME) (Rudnick et al. 2003; Rainville and Pinkel 2006a,b). The *FLIP* data combine CTD and Doppler sonar measurements to provide profiles of temperature, density, and horizontal and vertical velocity, covering a depth range of 80–800 m with 2–4-m vertical resolution. The 4-min profiling interval allows us to resolve the entire frequency range for internal waves, from the inertial frequency to the buoyancy frequency. We attempt to quantify nonlinear energy transfer rates through the triple correlation between high-frequency wave stresses and low-frequency wave shears. Bispectral analysis is used to identify specific frequencies and wavenumbers of triads whose interactions contribute to the energy transfers.

In the next section, we begin with a brief description of the instrumentation. Samples of the depth–time series of isopycnal displacements and horizontal velocities are presented and contrasted with vertical velocities and vertical shears. Spectral estimates are presented to establish the important frequencies and scales of motion. We then develop the basis for the triple correlation method and use it to estimate energy transfers at both HOME locations. Bispectral methods are explained and used to decompose the triple correlations by frequency and wavenumber. We attempt to sketch a picture of the interacting waves. Finally, we attempt to summarize the results and compare them to existing estimates of energy transfer and dissipation. A major result of the analysis is that a significant energy transfer from low-frequency to high-frequency waves is detected in both HOME Nearfield and Farfield. The interactions do not fit with preexisting notions of induced diffusion or elastic scattering at either location.

2. Instruments and data

Measurements were obtained near the Hawaiian Ridge during two 6-week deployments of the research platform *FLIP* as part of HOME. A map showing both locations is shown in Fig. 1. During the 2002 HOME Nearfield program, R/P *FLIP* was moored at 21.68°N, 158.63°W, on the southwest shoulder of Kaena Ridge. This ridge, formed by the northwest extension of the island of Oahu, was one of the most energetic tidal conversion sites identified during HOME. Shear levels 4 times greater
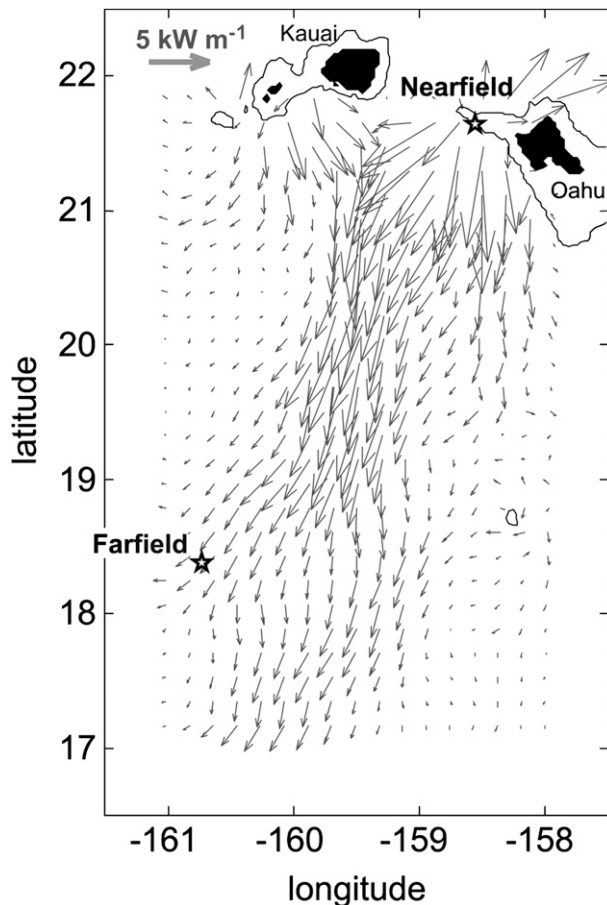
FIG. 1. Deployment of R/P *FLIP* in 2001–02 (Rainville and Pinkel 2006a). As part of HOME, *FLIP* was moored at two locations near Kaena Ridge, Hawaii. During the 2002 Farfield component, the measurement location was approximately 430 km to the southwest of the ridge crest, in the approximate path of an M_2 tidal beam (model fluxes are shown by the arrows). The 2002 Nearfield component placed *FLIP* on the shoulder of Kaena Ridge in approximately 1100 m of water, in a location intersecting the southward-propagating ray emanating from the north ridge.
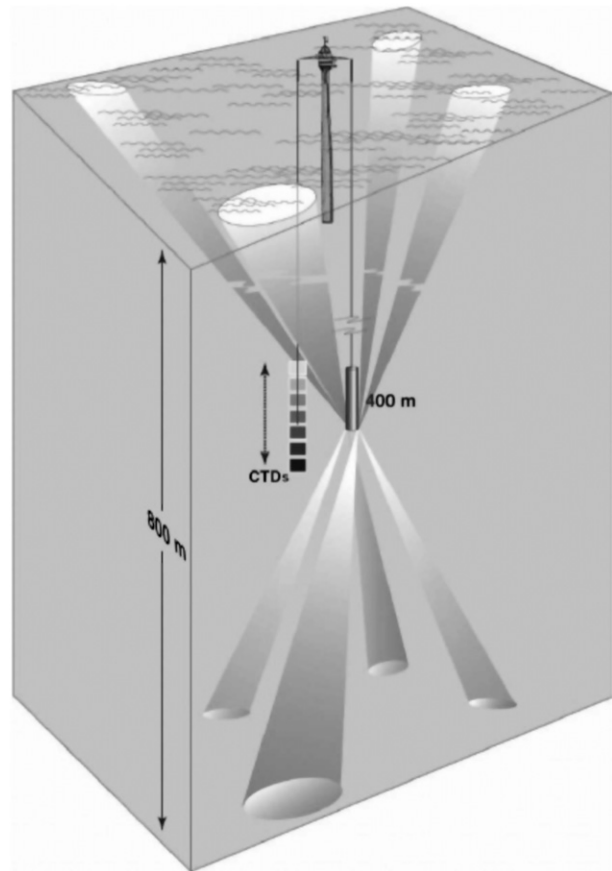

FIG. 2. Schematic of R/P *FLIP* instrumentation during HOME, 2001–02. Tandem Seabird SBE11 CTDs profiled down to approximately 800 m once every 4 min with approximately 2-m resolution. The Deep-8 Doppler sonar recorded horizontal velocities with approximately 4-m vertical resolution. Vertical velocities were inferred from the motion of isopycnals as measured by the CTDs. More than 11 000 profiles were collected during the Nearfield and more than 9000 were collected during the Farfield.

and vertical displacements 10 times larger than open-ocean levels were reported near the ridge (Rudnick et al. 2003; Rainville and Pinkel 2006a). In the 2001 HOME Farfield component, *FLIP* was deployed 430 km to the south-southwest of Oahu, at 18.39°N, 160.70°W, in the approximate path of an M_2 tidal beam emanating from Kaena Ridge. Here, wave energy levels were found to be more representative of the open ocean (Rainville and Pinkel 2006b).

The same instrumentation was used for both deployments (Fig. 2). A pair of Seabird SBE11 CTDs, sampling at 24 Hz and profiling at approximately 3.6 m s^{-1}, combined to record temperature and salinity over a depth range of 10–800 m once every 4 min with a vertical resolution of 2 m. Vertical velocities were inferred from the

motion of isopycnal surfaces, as estimated from the CTD record.

Horizontal velocities were measured by the Deep-8 Doppler sonar, which was deployed at 400-m depth in the Nearfield and 320-m depth in the Farfield. The Deep-8 was equipped with four upward-looking and four downward-looking beams, transmitting repeat-sequence coded pulses every 2 s and achieving a vertical resolution of 4 m (Pinkel and Smith 1992). The reader is referred to Rainville and Pinkel (2006a) for a more detailed discussion of the instruments and deployment.

Approximately 12 000 CTD profiles, spanning 33 days, were recorded in the 2002 Nearfield component. Nearly 10 000 profiles were taken over a 28-day span during the 2001 Farfield component.
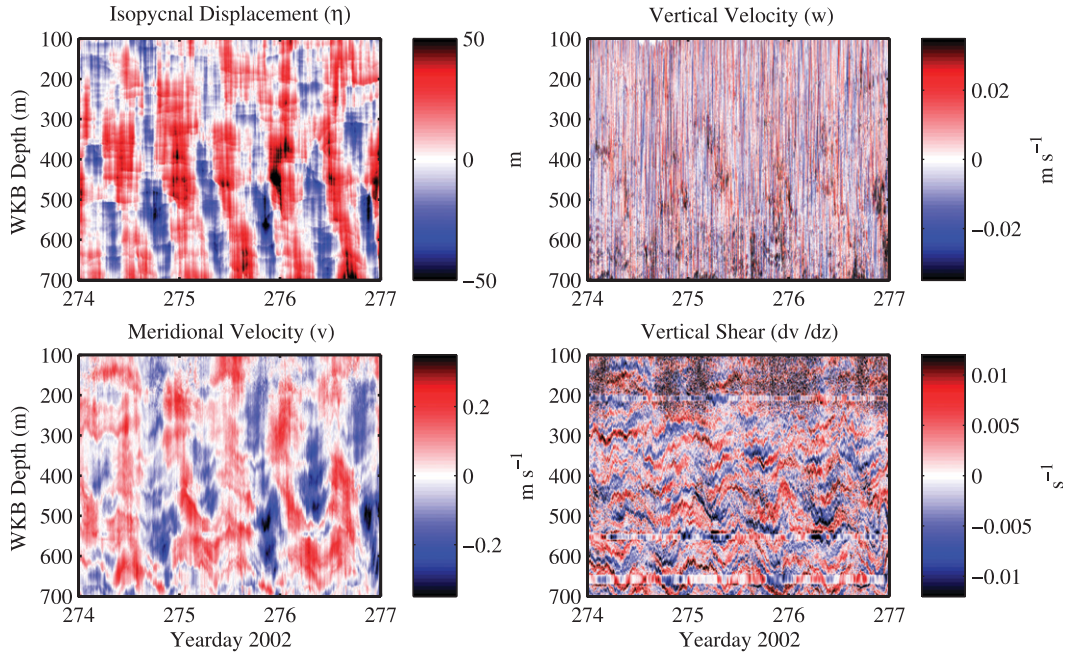
FIG. 3. HOME Nearfield: depth–time maps. Example 3-day windows of the Nearfield data are shown, emphasizing different spatial and temporal scales. Plots are WKB-scaled (4) and WKB-stretched (5). (top left) Isopycnal displacement η: long vertical scales and predominantly downward phase propagation with semidiurnal period are dominant. (top right) Vertical velocity w: high-frequency motions with long vertical scales are most apparent here. (bottom left) Meridional velocity v: a mix of semidiurnal and diurnal frequencies can be seen, with a greater mix of vertical scales than in w. (bottom right) Vertical shear $\partial v/\partial z$: much smaller vertical scales are apparent here than in the other records. Shear layers are visibly deformed by the vertical heaving of the tides. The Deep-8 sonar was deployed at 400 m (550 m in the WKB-stretched coordinate), resulting in a gap between 544- and 557-m depths in the record. Bands in depths of 203–214 m and 645–666 m are caused by surface and bottom reflections, respectively, in the sonar data. The gaps and discontinuities were interpolated in the velocities but are still apparent in the shears.

a. Depth–time maps

Example 3-day windows of isopycnal displacement, horizontal and vertical velocities, and vertical shears from each location are presented in Figs. 3 and 4. To allow a better visual comparison between depths, Wentzel–Kramers–Brillouin (WKB)-scaled vertical coordinates (Gill 1982) have been used at each site. A cruise-averaged profile of the buoyancy frequency $N(z)$ defines the scaled coordinate,

$$z_{\text{WKB}} = \frac{1}{N_0}\int_0^z N(z')\,dz', d, \qquad (4)$$

where the constant N_0 has been chosen so that z_{WKB} spans the same profiling range as the original coordinate z.

Velocities and shears have also been scaled,

$$w = w_0\left(\frac{N}{N_0}\right)^{1/2}, \quad (u,v) = (u_0,v_0)\left(\frac{N}{N_0}\right)^{-1/2},$$

$$(u_z,v_z) = ((u_0)_z,(v_0)_z)\left(\frac{N}{N_0}\right)^{-1}, \qquad (5)$$

where each subscript 0 indicates the original quantity. The scaling for linear propagation has been used for velocities, but observed shears at both locations were found to vary nearly as N rather than the predicted $N^{3/2}$, so a scaling of $(N/N_0)^{-1}$ is used for the shears.

Several vertical discontinuities exist in the sonar data and are most visible in the shears. There is a gap around the Deep-8, due to the separation between the upward-looking and downward-looking sonar records, which appears at depths of 544–557 m in the Nearfield and 483–502 m in the Farfield. Reflections from the sea surface contaminate depths of 203–214 m and 177–200 m, respectively. A bottom reflection, which appears only in the Nearfield, is also present in depths of 645–666 m. To minimize the effect of these vertical discontinuities, Eulerian coordinates are used through the present study. This departs from the approach of Rainville and Pinkel (2006a) and others, who have used semi-Lagrangian (isopycnal) coordinates to reduce the effects of vertical advection by the semidiurnal tide. In the conversion to a semi-Lagrangian frame, the sonar artifacts are spread across all isopycnals that pass through the affected
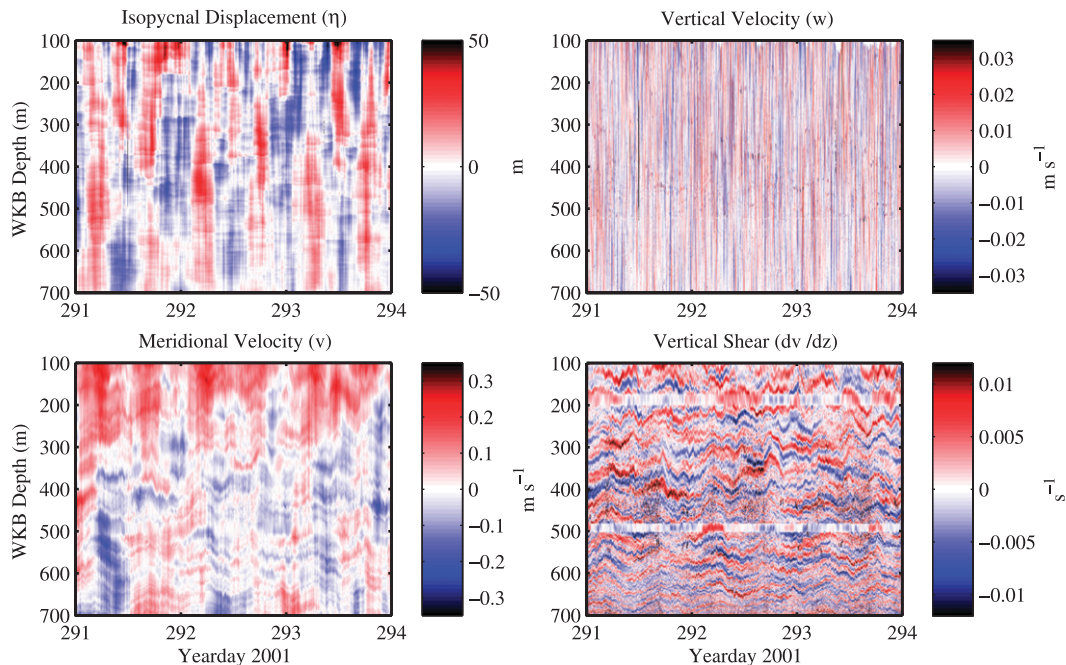
FIG. 4. HOME Farfield: depth–time maps. As in Fig. 3, but for the Farfield. (top left) Isopycnal displacement η: long vertical scales are evident but no dominant sense of vertical propagation is seen. (top right) Vertical velocity w: high-frequency motions with long vertical scales are seen as in the Nearfield. (bottom left) Meridional velocity v: a mix of scales is seen, with less visible similarity to η. (bottom right) Vertical shear $\partial v/\partial z$: as before, small vertical scales with significant layer deformation are seen. Here the Deep-8 sonar was deployed at 320 m (490 m in the WKB-stretched coordinate), resulting in a gap between 483- and 502-m depths in the record. The band in depths of 177–200 m is caused by a surface reflection in the sonar data. The gaps and discontinuities were interpolated in the velocities but are still apparent in the shears.

depths. By remaining in the Eulerian frame, we limit the influence of the artifacts. We have carried out a parallel, semi-Lagrangian analysis and find that the results reported here are not significantly affected by the coordinate choice. For visual presentation, the Eulerian velocity data have been interpolated across the affected depths, but the interpolated depths are discarded whenever statistical averages are subsequently formed.

Not seen in the figures is a brief interruption to CTD profiling that occurred in the Nearfield around day 280 of 2002, when one of the CTDs collided with the Deep-8. Profiling resumed with a reduced, 700-m maximum depth.

The quantities from the Nearfield, shown in Fig. 3, display different spatial and temporal scales. Displacements η (top left) exceed 100 m in the maximum and are dominated by waves with long vertical scales and approximately semidiurnal period. A pronounced downward phase propagation of wave crests indicates predominantly upward energy propagation. These features are the signature of the semidiurnal internal tide emanating upward from the ridge, as discussed in Rainville and Pinkel (2006a). A local maximum in displacement appears between 350 and 500 m in stretched coordinates and is

associated with a tidal beam that crosses the profiling column near those depths.

Meridional velocities v (Fig. 3, bottom left), which are approximately cross-ridge in the Nearfield, largely resemble the displacements. Peak magnitudes are approximately 25 cm s^{-1}. The period is still predominantly semidiurnal, but a more complicated vertical structure is visible in addition to the low-mode pattern seen in the displacements.

Vertical velocities w (Fig. 3, top right) and vertical shears v_z (Fig. 3, bottom right) show opposite extremes in scale. Only a hint of the semidiurnal wave crests in η are visible in w. Instead, the record is filled by much higher-frequency motions, with some motion at short scales but much of it at long wavelengths. In contrast, fine vertical scales on the order of 100 m and low frequencies dominate the shear record. Although hints of semidiurnal and near-inertial phase variations can be seen following shear layers, the most prominent visual effect is that of vertical heaving of the shear layers associated with the semidiurnal tide.

The Farfield displacements η, presented in Fig. 4 (top left), also have relatively long vertical scales as seen in
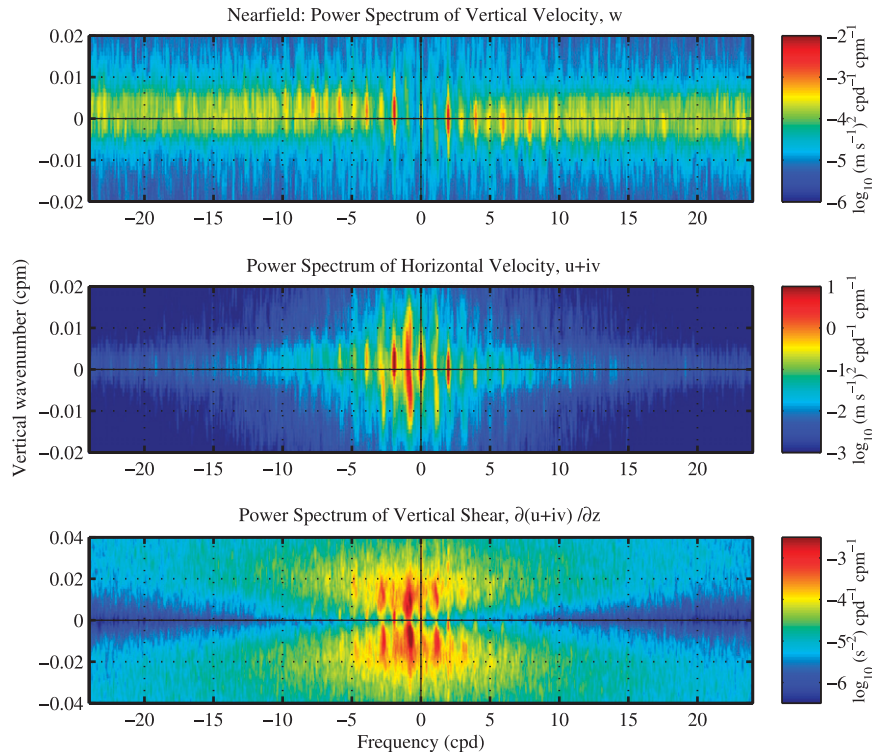
FIG. 5. HOME Nearfield: frequency–wavenumber spectra. Positive (negative) wavenumbers denote upward- (downward-) propagating wave energy. (top) Vertical velocity w: most of the variance is concentrated near $M_2 = 1.93$ cpd and a set of apparent tidal harmonics, all of which are predominantly associated with up-going wave energy. The spectrum gradually becomes more symmetric with respect to vertical propagation at frequencies greater than about 12 cpd. (middle) Complex horizontal velocity $(u + iv)$: near-inertial and semidiurnal variance is apparent, along with the first few tidal harmonics. (bottom) Complex vertical shear $(u + iv)_z$: here, variance is concentrated in the near-inertial peak. More near-inertial energy is going downward than upward. The K pattern that broadens with wavenumber is due in large part to Doppler shifting of low-frequency waves by the vertical motions of the tides.

the Nearfield, but here the displacements show no clear sense of vertical phase propagation. This is consistent with the view that the internal tide gradually assumes a low-mode structure as it propagates away from the generation site. Rainville and Pinkel (2006a) reported that nearly all the semidiurnal variance at the Farfield site was contained in the first three modes, with more than 60% in mode 1.

Velocities v in the Farfield (Fig. 4, bottom left) also show a mix of longer vertical scales and shorter-wavelength features, but unlike in the Nearfield there is limited resemblance between η and v. In particular, a series of shorter-scale motions visible below 300 m in the Farfield have much smaller scales than seen here above 300 m or in any part of the water column in the Nearfield.

Vertical shears in the Farfield (Fig. 4, bottom right) show finer vertical scales and a somewhat more coherent wave group structure than in the Nearfield. It is difficult

to visually identify a dominant oscillation period. As before, vertical velocities w (Fig. 4, top right) show a slight hint of the structures seen in η embedded in a field of high-frequency motions.

b. Spectral estimates

The full depth–time records of WKB stretched and scaled data are two-dimensional (2D) Fourier transformed after applying a 5% Tukey taper in both depth and time to reduce spectral leakage. Raw variances are smoothed by a 3 bin $\times$ 5 bin moving average, corresponding to approximately 0.003 cpm in vertical wavenumber $\times$ 0.1 cpd in frequency, to produce the vertical wavenumber–frequency (κ, ω) power spectra shown in Figs. 5 and 6. Horizontal velocities were combined in complex form $u + iv$ to produce rotary power spectra. As a result of our sign convention, spectral variance in quadrants II and IV (where frequency and vertical wavenumber have opposite sign) corresponds to
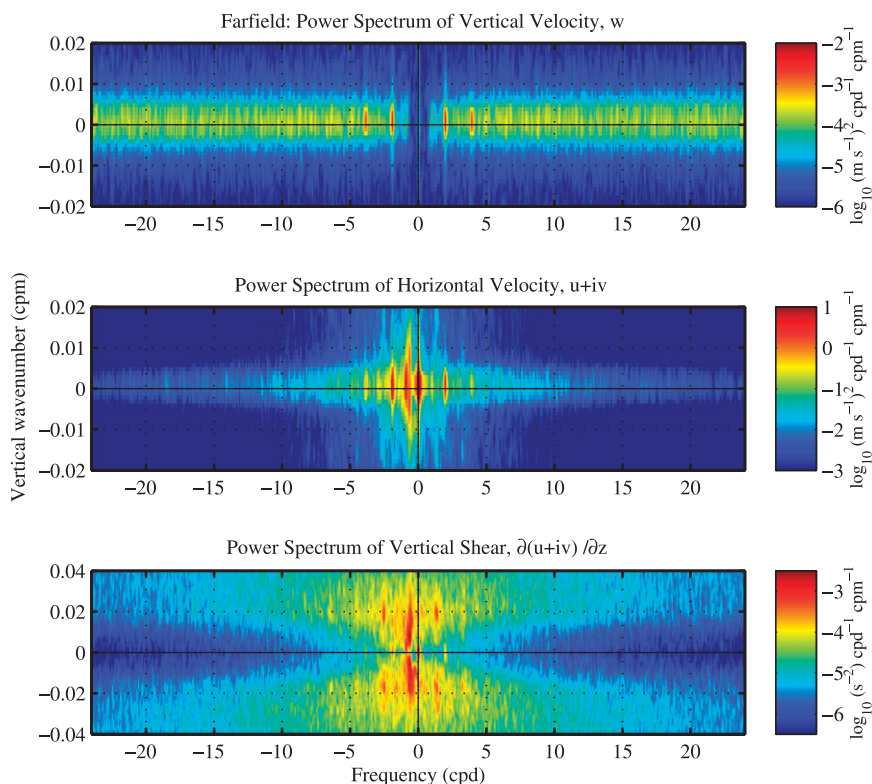
FIG. 6. HOME Farfield: frequency–wavenumber spectra. As in Fig. 5, but for the Farfield. Positive (negative) wavenumbers denote upward- (downward-) propagating wave energy. (top) Vertical velocity w: only the semidiurnal tidal frequency and its first harmonic are clearly identifiable. Vertical energy propagation is roughly symmetric. (Middle) Complex horizontal velocity $(u + iv)$: near-inertial and semidiurnal variance is apparent here. (Bottom) Complex vertical shear $(u + iv)_z$: variance is concentrated in the near-inertial peak, with roughly equal parts going upward and downward. The K pattern that is due in large part to Doppler shifting of low-frequency waves by the tides is visible here as well.

upward-propagating wave energy, while quadrants I and III (where frequency vertical wavenumber and frequency have the same sign) show downward-propagating wave energy.

In the Nearfield spectra, shown in Fig. 5, vertical velocities (Fig. 5, top) show a progression of vertical ridges that are nearly symmetric about the origin and associated with predominantly upward energy propagation. The strongest ridges are associated with the low-mode internal tide at the principal lunar semidiurnal frequency, $\pm M_2 = \pm 1.93$ cpd, corresponding to a period of 12.42 h. Harmonics of the tide are also evident at $\pm 2M_2$, $\pm 3M_2$, $\pm 4M_2, \ldots$ The distinction between M_2 and the solar semidiurnal frequency, $S_2 = 2.0$ cpd, is apparent by the fourth harmonic of M_2, at 9.66 cpd. A series of lesser ridges can be seen between the M_2 harmonics and may be Doppler-shifted images of the M_2 harmonics. The extension of the ridges at nM_2 frequency to small downward wavenumbers may be due in part to spectral leakage from the upward half plane. The asymmetry

gradually subsides with increasing frequency, so that waves above 12 cpd have roughly equal upward and downward variance. Outside of the large peaks, variance appears relatively constant with increasing frequency.

The largest horizontal velocity variances are found near $\pm M_2$ frequency, again at small wavenumbers and with a distinctly upward sense of propagation. Variance at near-inertial frequencies rolls off more slowly with wavenumber than does the tide and is associated with both upward and downward waves. The downward near-inertial ridge contains somewhat more variance and peaks at slightly lower frequency than the upward ridge. A smaller ridge is also apparent at approximately $-(1/2)M_2$ frequency and is concentrated at somewhat smaller wavenumbers than the near-inertial variance. A downward ridge of unknown origin is seen at about -3 cpd. Overall, the horizontal velocity spectra roll off quickly with frequency, and in the more apparent lower frequencies, somewhat more upward than downward energy is seen as in the power spectra of w.
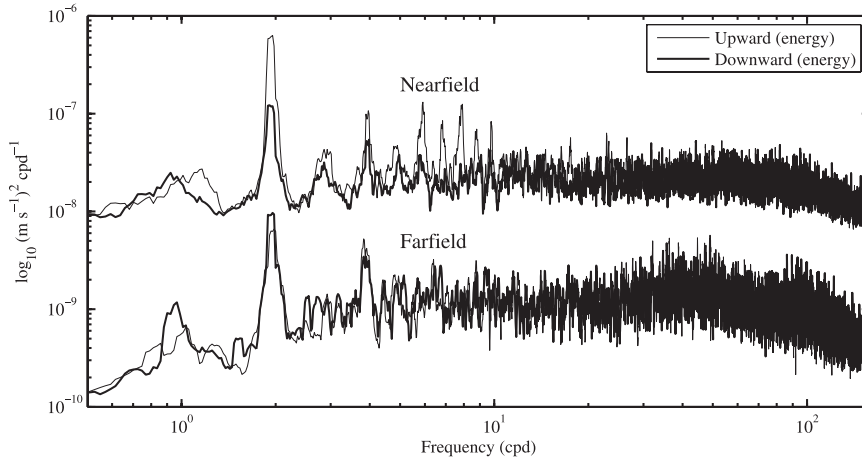
FIG. 7. Frequency spectra of vertical velocity. The top spectrum is Nearfield w: excess upward-propagating wave energy is visible at the semidiurnal frequency M_2, a series of harmonics, and at the subharmonic $(1/2)M_2$. The bottom spectrum is Farfield w: the Farfield spectrum has been shifted down by one order of magnitude. There is little if any vertical asymmetry visible in the Farfield.

Shear variance is concentrated at a near-inertial peak, with wavenumbers $\approx \pm 0.01$ cpm associated with downward propagation. Significant but lesser variance is also associated with upward near-inertial propagation. The peak at $-(1/2)M_2$ frequency is more distinct in the shear spectra. Note the expanded wavenumber limits in the shear plot relative to the velocity spectra to accommodate the decreased slope with increasing wavenumber. Despite the change in slope, shears still fall off above about 0.025 cpm. A widening pattern of shear variance is apparent with increasing vertical wavenumber. This "hourglass" shape is associated with Doppler shifting in these Eulerian wavenumber–frequency spectra (Pinkel 2008).

In contrast to the Nearfield, the Farfield spectra are not noticeably asymmetric with respect to vertical propagation. Farfield vertical velocity variance (Fig. 6, top) is confined to small wavenumbers as in the Nearfield. Distinct lines appear at frequencies $\pm M_2$ and $\pm 2M_2$, but $\pm 3M_2$ and $\pm 4M_2$ are difficult to distinguish from the background. Horizontal velocity spectra also show a low-mode M_2 tide. A better separation between f and $(1/2)M_2$ is seen in the Farfield because of the slightly lower local inertial frequency. Shear variance is mainly distributed near the inertial frequency.

Frequency spectra are obtained by integrating the spectral variance in Figs. 5 and 6 over all vertical wavenumbers. Vertical velocity spectra from both the Nearfield and Farfield are presented together for comparison in Fig. 7. Upward- and downward-traveling energy are overplotted on the same log–log axes. The Farfield spectra (lower plots in each panel) have been shifted downward by one order of magnitude for visual clarity. The ridges in upward energy in the Nearfield are visible here as sharp peaks in the upper plots, with the upward semidiurnal variance about 5 times as large as the downward variance. The Nearfield variances remain relatively steady with rising frequency, with a hint of a rolloff before 10^2 cpd, whereas the Farfield variances appear to rise slightly before beginning a rolloff at slightly lower frequency. A sharp rolloff is not seen in either plot because the spectra represent an average of frequency spectra from depths across which N varies by a factor of 3–4.

Horizontal velocities and vertical shears (Fig. 8) tell much the same story. The Nearfield semidiurnal velocity peak is nearly an order of magnitude larger in upward variance than in downward variance, and the upward tidal harmonics are distinct until about 10 cpd. However, downward near-inertial shear variance is somewhat larger than upward near-inertial shear variance. The Farfield spectra, by contrast, are quite symmetric in all respects.

Vertical wavenumber spectra, shown in Fig. 9, are obtained by integrating the wavenumber–frequency spectra across all frequencies. Our ability to resolve vertical wavenumbers is limited relative to our ability to resolve frequencies. Low wavenumber resolution is limited by the profiling range, which was about 600 m in the vertical. Vertical velocity variance, shown in the left panel of Fig. 9, is concentrated at the two lowest wavenumbers that could be resolved, with a falloff of approximately $m^{-3/2}$ in the Nearfield and a somewhat
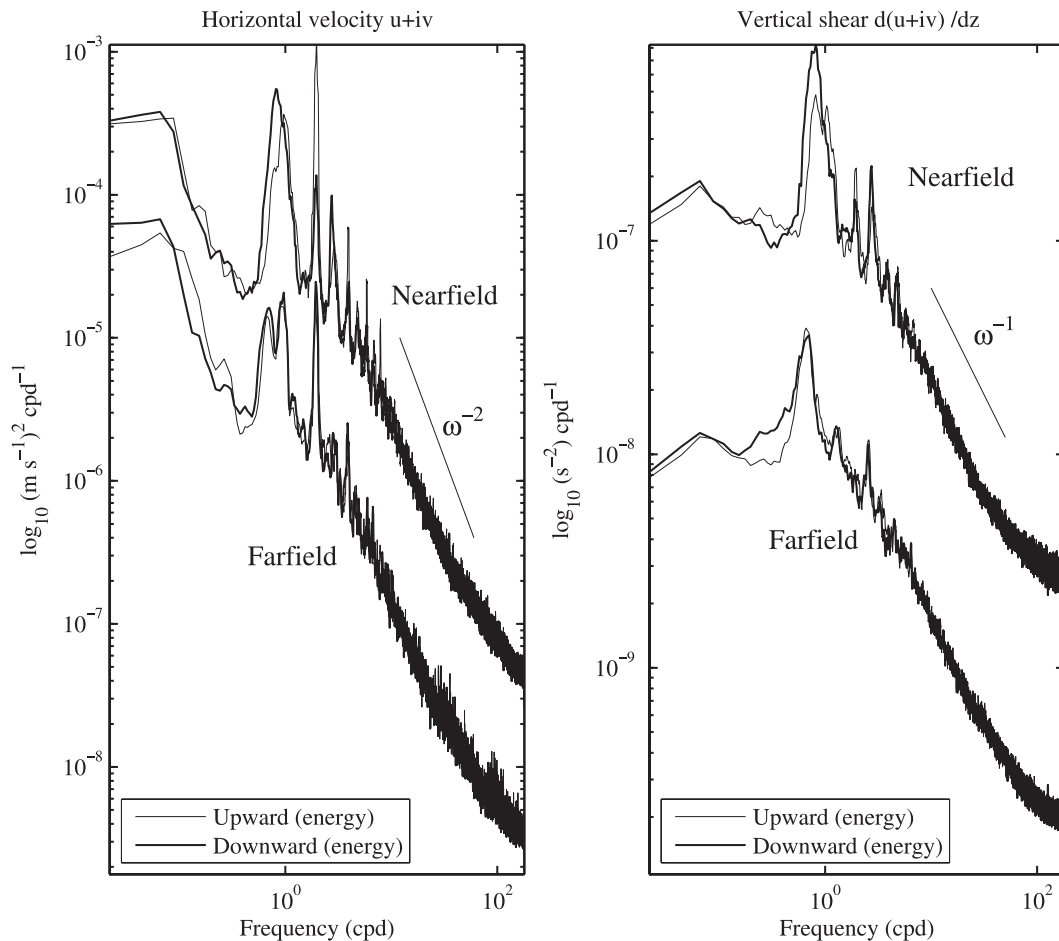
FIG. 8. Frequency spectra of horizontal velocity and vertical shear. As before, the Farfield spectra have been shifted down by one order of magnitude. (Left) Complex horizontal velocity $(u + iv)$: the series of tidal harmonic peaks are visible in the Nearfield, with excess up-going energy. In the Farfield, the near-inertial and diurnal peaks are resolved. The semidiurnal peak is accompanied by only one or two significant harmonics. (right) Complex vertical shear $(u + iv)_z$: here, similar features are seen as in the velocity spectra, but the near-inertial peak is greatly emphasized. Only near-inertial shears are markedly unequal in the Nearfield, with more wave energy propagating downward.

steeper $m^{-5/2}$ in the Farfield. The wavenumber spectra are much smoother than the frequency spectra because of the large number of profiles that have been averaged. The slope steepens in the Nearfield above wavenumbers of about 3×10^{-2} cpm. The Farfield variance flattens out briefly around 1×10^{-2} cpm before falling off more steeply again above 7×10^{-2} cpm.

The vertical shear wavenumber spectra, shown on the right panel of Fig. 9, are relatively similar between the two sites. The Farfield shear variance peaks at about $\frac{1}{60}$ cpm, whereas variance in the Nearfield peaks at a slightly lower wavenumber, about $\frac{1}{90}$ cpm. Shear variance falls off on both sides of the peak wavenumber in all the spectra except the Nearfield downward, where the peak is broadened into a plateau between about $\frac{1}{200}$ and $\frac{1}{90}$ cpm.

3. Stress–shear triple correlation

Products of the form $\langle u_i' u_j' \rangle \partial U_i / \partial x_j$, where $\partial U_i / \partial x_j$ represents a mean strain rate and the $\langle u_i' u_j' \rangle$ are time-averaged Reynolds stresses, are familiar as the shear production term from turbulence theory (Tennekes and Lumley 1972). Studies of wave–mean flow interactions have also examined analogous correlations, in which the stresses are presumed to be due to wave activity rather than turbulent motions and the mean strain rates are assumed to be primarily vertical shears (Ruddick and Joyce 1979; Gargett and Holloway 1984; Jacobs and Cox 1987; Duda and Jacobs 1998).

Our method for demonstrating energy transfers between the energetic low-frequency shears and higher-frequency waves focuses on triple correlations of the form
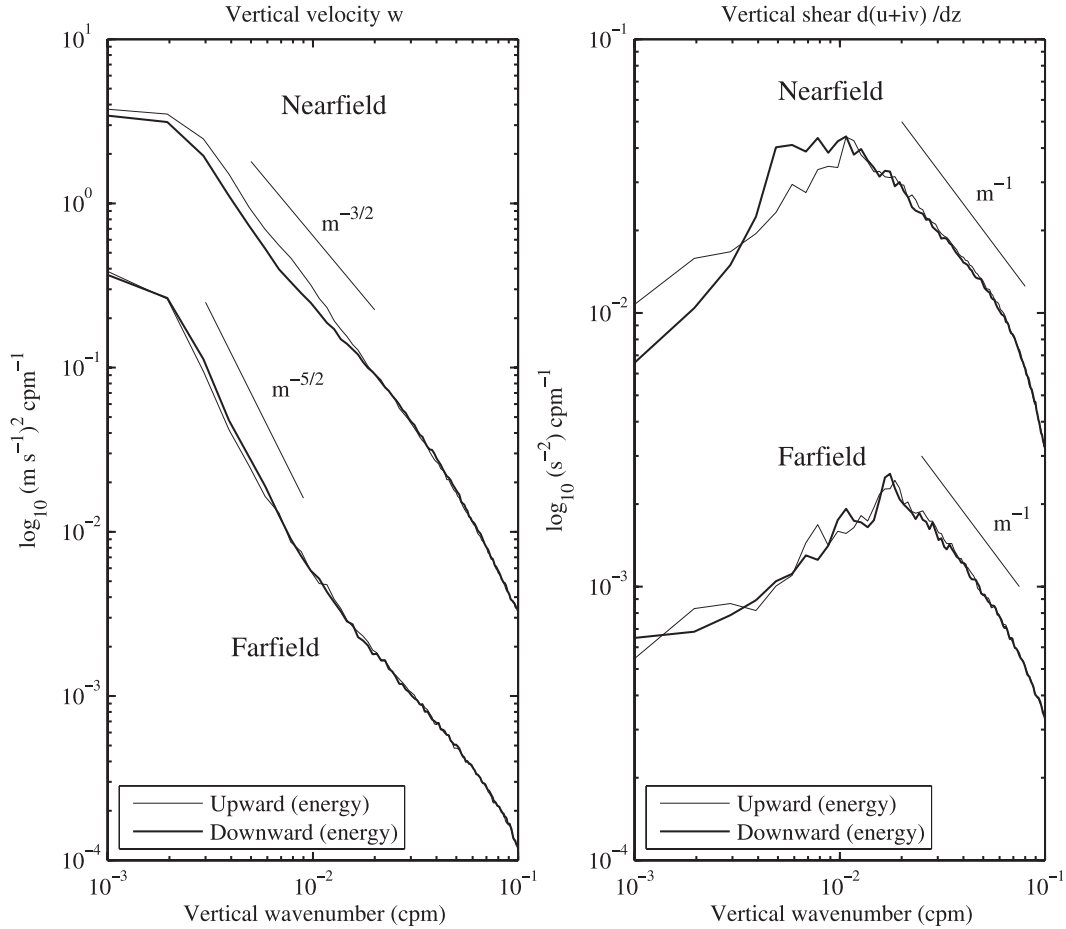
FIG. 9. Wavenumber spectra of vertical velocity and shear. As before, the Farfield spectra have been shifted down by one order of magnitude. (Left) Vertical velocity w: variance is concentrated in the lowest few wavenumber bins. The Farfield velocity rolls off more steeply with vertical wavenumber before about 10^{-2} cpm, relative to the Nearfield. (bottom) Vertical shear $(u + iv)_z$: the Farfield spectra are sharply peaked at $1/60$ cpm. The Nearfield peak in up-going energy is at $1/90$ cpm. Down-going energy in the Nearfield is extended in a band between $1/200$ and $1/90$ cpm. Spectra have not been corrected for the 4-m centered differencing used to calculate shears.

$$\left\langle u_i' w' \frac{\partial U_i}{\partial z} \right\rangle, \quad i, j = 1, 2, \qquad (6)$$

where as before the angle brackets $\langle \cdot \rangle$ indicate time averaging. Unlike in the turbulent production term, the $\partial U_i/\partial z$ in (6) are not mean shears but instead oscillate at low frequency. Meanwhile, the "fluctuation" stresses $u_i' w'$ are associated with motions at higher frequencies than the $\partial U_i/\partial z$ and are assumed, but not required, to be internal waves. We differ from Duda and Jacobs (1998) and others by not explicitly assuming a vertical scale separation between the high-frequency waves and the low-frequency shears.

To relate the triple product (6) to an energy transfer between low- and high-frequency waves, it is useful to return to the equations of motion,

$$\frac{\partial \mathbf{u}}{\partial t} + \mathbf{u} \cdot \nabla \mathbf{u} + f \times \mathbf{u} = -\nabla p / \rho_0 - \nabla \Phi, \qquad (7)$$

where $\mathbf{u} = (u, v, w)$ is the velocity vector in Cartesian components, f is the Coriolis frequency, p is pressure, Φ is the geopotential, and ρ_0 is the density profile at rest.

We proceed by writing the total flow as a sum of low- and high-frequency parts,

$$\mathbf{u} = \mathbf{U} + \mathbf{u}', \quad p = \tilde{p} + p', \quad \rho = \tilde{\rho} + \rho'. \qquad (8)$$

An energy evolution equation for the high-frequency fluctuations is obtained by taking the scalar product of $\mathbf{u}'$ with (7) and time averaging over a period that is long compared to the time scales of both $\mathbf{u}'$ and $\mathbf{U}$,

$$\left\langle \frac{1}{2}\frac{\partial}{\partial t}\|\mathbf{u}'\|^2 \right\rangle + \left\langle \mathbf{u}' \cdot \frac{\partial \mathbf{U}}{\partial t} \right\rangle + \left\langle \mathbf{u}' \cdot [(\mathbf{U} + \mathbf{u}') \cdot \nabla(\mathbf{U} + \mathbf{u}')] \right\rangle$$

$$= \left\langle -\mathbf{u}' \cdot \frac{1}{\rho_0}[\nabla(\tilde{p} + p') + g(\tilde{\rho} + \rho')\hat{\mathbf{k}}] \right\rangle, \qquad (9)$$

where $\|\mathbf{u}'\|^2 = \mathbf{u}' \cdot \mathbf{u}'$ is the Euclidean norm.

Assuming a statistically steady state and no overlap in frequency between $\mathbf{U}$ and $\mathbf{u}$, the correlation between a low-frequency and a high-frequency quantity must vanish,

$$\left\langle \mathbf{u}' \cdot \frac{\partial \mathbf{U}}{\partial t} \right\rangle = 0, \quad \langle \nabla \tilde{p} \cdot \mathbf{u}' \rangle = 0, \quad \langle \tilde{\rho} w' \rangle = 0. \quad (10)$$

Next we expand the triple correlations, keeping only quadratic terms in the primed (high-frequency) quantities,

$$\langle \mathbf{u}' \cdot [(\mathbf{U} + \mathbf{u}') \cdot \nabla(\mathbf{U} + \mathbf{u}')] \rangle$$
$$= \langle \mathbf{u}' \cdot (\mathbf{U} \cdot \nabla \mathbf{U}) \rangle + \langle \mathbf{u}' \cdot (\mathbf{U} \cdot \nabla \mathbf{u}') \rangle + \langle \mathbf{u}' \cdot (\mathbf{u}' \cdot \nabla \mathbf{U}) \rangle. \qquad (11)$$

The first correlation on the right-hand side, $\langle \mathbf{u}' \cdot (\mathbf{U} \cdot \nabla \mathbf{U}) \rangle$, is formed by the product of one high-frequency and two low-frequency quantities. Triads interactions between these frequencies include PSI, particularly PSI involving semidiurnal tides and pairs of near-diurnal subharmonics. Such an interaction in HOME Nearfield is the subject of a companion paper (Sun and Pinkel 2012, manuscript submitted to *J. Phys. Oceanogr.*) and will not be addressed here. In this analysis, we avoid the influence of PSI by requiring a frequency gap of at least one octave between the low- and high-frequency fields. Any pair of low-frequency waves would be frequency resonant with a third wave whose frequency is too low to be found in the high-frequency field. The triple correlation $\langle \mathbf{u}' \cdot (\mathbf{U} \cdot \nabla \mathbf{U}) \rangle$ is thus zero. The second term, $\langle \mathbf{u}' \cdot (\mathbf{U} \cdot \nabla \mathbf{u}') \rangle = \mathbf{U} \cdot \nabla(1/2)\mathbf{u}'^2$, represents the advection of high-frequency kinetic energy by the low-frequency motions, which, unlike in the wave–mean flow problem, are assumed to be oscillatory, so that the net advection is zero. The remaining term, $\langle \mathbf{u}' \cdot (\mathbf{u}' \cdot \nabla \mathbf{U}) \rangle = \langle u_i' u_j' \partial U_i / \partial x_j \rangle$, is the triple correlation of interest that appears in (6).

Thus, using (10) and retaining the nonzero triple correlation in (11), the time-averaged energy equation (9) becomes

$$\left\langle \frac{\partial}{\partial t}\frac{1}{2}\|\mathbf{u}'\|^2 \right\rangle + \langle \mathbf{u}' \cdot (\mathbf{u}' \cdot \nabla \mathbf{U}) \rangle$$
$$= \left\langle -\frac{1}{\rho_0}\nabla \cdot (p'\mathbf{u}') \right\rangle - \left\langle \frac{g}{\rho_0}\rho' w' \right\rangle. \qquad (12)$$

The first and last terms have the familiar forms of the time derivatives of averaged kinetic and potential energy densities,

$$\frac{\partial \langle E_k' \rangle}{\partial t} = \left\langle \frac{\partial}{\partial t}\frac{1}{2}\|\mathbf{u}'\|^2 \right\rangle, \quad \frac{\partial \langle E_p' \rangle}{\partial t} = \frac{1}{\rho_0}\langle g\rho' w' \rangle, \quad (13)$$

whose sum we define as the total averaged energy density,

$$\langle E' \rangle = \langle E_k' \rangle + \langle E_p' \rangle. \qquad (14)$$

Thus, using index notation for the triple correlation, (12) can be expressed as

$$\frac{\partial \langle E' \rangle}{\partial t} = -\left\langle u_i' u_j' \frac{\partial U_i}{\partial x_j} \right\rangle - \frac{1}{\rho_0}\nabla \cdot \langle p'\mathbf{u}' \rangle, \qquad (15)$$

which represents an energy balance between the high-frequency source $-u_i' u_j' \partial U_i / \partial x_j$ and the divergence of energy flux due to high-frequency waves. For $\mathbf{u}'$ composed of a high-frequency wave packet with energy density E' and group velocity $\mathbf{c}_g'$, the energy flux is

$$\frac{1}{\rho_0}(p'\mathbf{u}') = \mathbf{c}_g' E', \qquad (16)$$

so that (15) has the interpretation

$$\frac{\partial \langle E' \rangle}{\partial t} + \nabla \cdot \mathbf{c}_g' \langle E' \rangle = -\left\langle u_i' u_j' \frac{\partial U_i}{\partial x_j} \right\rangle, \qquad (17)$$

in which $\langle -u_i' u_j' \partial U_i / \partial x_j \rangle$ balances the change in average energy $\langle E' \rangle$ in a frame moving with the group velocity.

Generally, the low-frequency vertical shears are thought to dominate over the horizontal shears. Unfortunately, we have no direct way of evaluating the correlations $\langle -w' u_i' \partial W / \partial x_i \rangle$ involving horizontal stresses and horizontal velocity gradients. Horizontal homogeneity of the internal wave field is sometimes invoked to justify dropping the horizontal stress–shear terms (Gargett and Holloway 1984), but here such an assumption may be problematic because the wave field in the Nearfield is characterized by horizontally inhomogeneous features such as tidal beams. Keeping these difficulties in mind, we proceed by retaining only the correlations involving low-frequency vertical shears and assign them the symbol

$$\varepsilon_* = -\left\langle u_i' w' \frac{\partial U_i}{\partial z} \right\rangle, \quad i = 1, 2, \qquad (18)$$

to emphasize the analogy between our high-frequency source term and the turbulent shear production term.

An associated correlation coefficient r_*, which measures the relative coupling between the waves contributing to
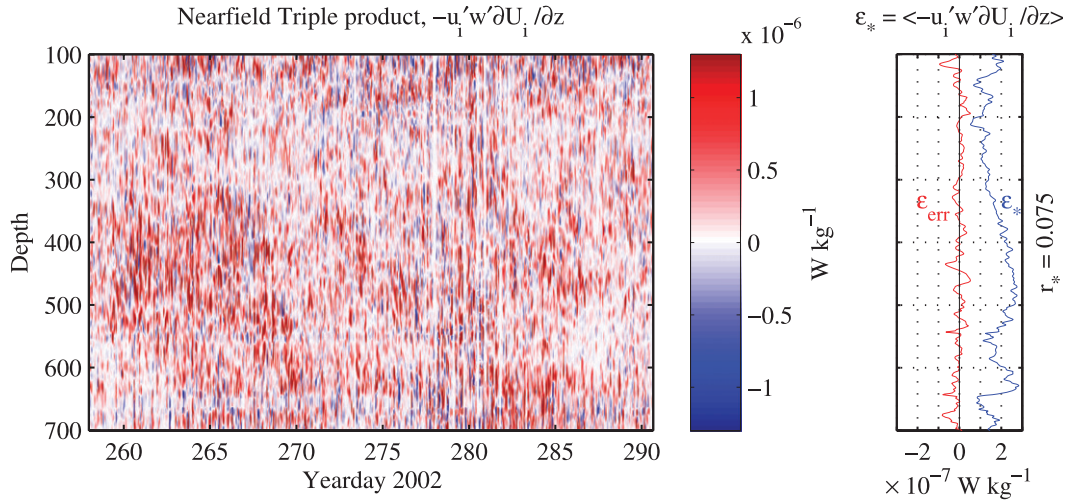
FIG. 10. Nearfield: stress–shear triple product. (left) Triple product ($-u_i w \partial U/\partial z$): red patches indicate positive energy transfer from low-frequency shears to high-frequency waves. Most of the activity occurs between 400- and 600-m depth, where the shear maximum is located and also roughly where a tidal beam crosses the profiling column. (right) Energy transfer rate ε_*: the blue line is a profile of ε_*, the time-averaged energy transfer rate. The red line ε_{err} is an error estimate calculated using the unaligned horizontal terms.

ε_* independent of their respective energy levels, can be defined by normalizing ε_* by the root-mean-square (RMS) magnitude,

$$r_* = \frac{\varepsilon_*}{\sqrt{\langle (u_i')^2 \rangle \langle (w')^2 \rangle \langle (\partial U_i/\partial z)^2 \rangle}}. \quad (19)$$

Estimates of ε_* in HOME

Depth–time maps of high-frequency u_i' and w' and low-frequency ($\partial U_i/\partial z$) in both HOME locations are formed from WKB stretched and scaled quantities. To obtain ($\partial U_i/\partial z$), the vertical shears are filtered in frequency to allow a passband of $\frac{1}{40}$–$\frac{1}{8}$ cph, or 0.6–3 cpd, which includes the most of the shear in the inertial, diurnal, and semidiurnal bands as seen in the spectra of Fig. 8. Meanwhile, w and u_i are high-pass filtered above 6 cpd, leaving a frequency gap to exclude PSI-like interactions. All filters are zero-phase, sixth-order Butterworth. To form the triple products that appear inside the brackets in (18), the bandpassed u_i', w', and ($\partial U_i/\partial z$) are multiplied together pointwise and summed over the index i.

Depth–time maps of $-u_i'w'(\partial U_i/\partial z)$ are shown in Figs. 10 and 11. The plots have been smoothed by 10 m in depth and 1 h in time. A patch of predominantly red color is apparent in the Nearfield triple product (Fig. 10) below 300-m depth on days 260–270. The relatively uniform color indicates sustained interactions resulting in a positive net energy transfer from low-frequency shears to high-frequency waves. The patch is strongest

between spring semidiurnal tide and the maximum of near-inertial variance around day 270. Between days 276 and 287, more red streaks and patches are visible below 300 m, including a deeper patch below 550 m on days 281–286. There is a band of relative quiet between approximately 150- and 300-m depths, part of which is due to the surface reflection in the sonar data near 200 m, above which there are more active interactions.

The profile of ε_*, plotted to the right of the main plot, is a time average of triple products. Physical units of energy transfer rate per unit mass are preserved by computing averages from raw, rather than WKB-scaled, quantities. The energy transfer rate in the Nearfield, calculated as a simple average over depth (non–WKB scaled) using unscaled quantities, is about 2×10^{-7} W kg^{-1}, with a maximum value of 2.8×10^{-7} W kg^{-1} near a depth of 630 m. The correlation r_* (not shown) has a similar profile to ε_* but scaled by a constant, with a depth-averaged r_* of 0.075.

Measurement error is a concern in the energy transfer estimates. To provide an intuitive estimate of the error, we compute a test correlation ε_{err} from velocities and shears that have the same magnitudes as in ε_* but are unaligned and thus are not physically meaningful,

$$\varepsilon_{err} = -\left\langle u_i'w'\frac{\partial U_j}{\partial z} \right\rangle, \quad i,j = 1,2, i \neq j. \quad (20)$$

The error estimates ε_{err}, plotted on the same axes as the ε_* profile, are found to be smaller than ε by about an order of magnitude.
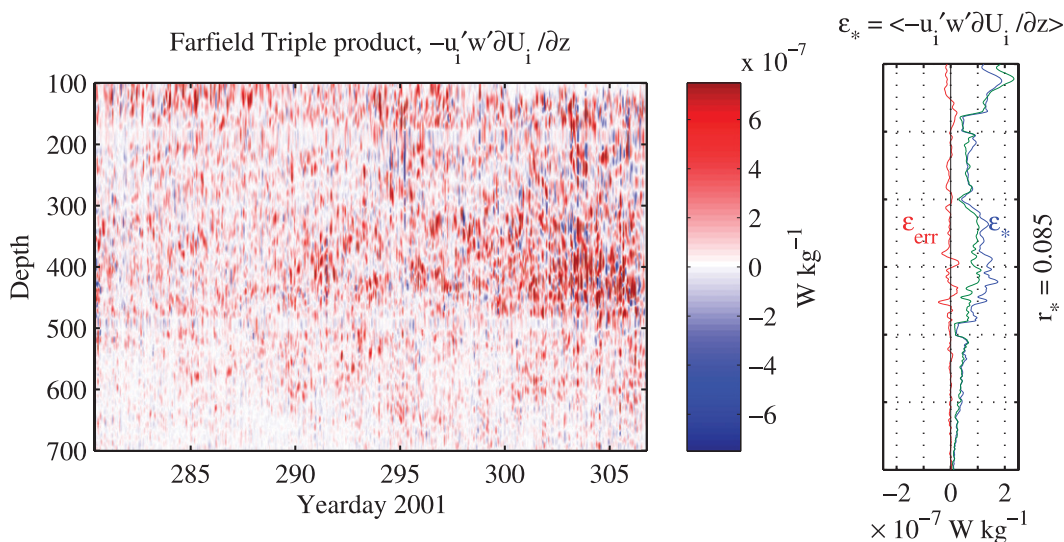
FIG. 11. Farfield: stress–shear triple correlation. As in Fig. 10, but for the Farfield. (left) Triple product ($-u_i w \partial U_i /\partial z$): red patches, indicating positive energy transfer from low-frequency shears to high-frequency waves, are more sparse here than in the Nearfield. The burst of energy after day 300 may be associated with an eddy that passed through the measurement site. (right) Energy transfer rate ε_*: the blue line is a profile of ε_*, the time-averaged energy transfer rate. The green line is ε_* computed using only data prior to day 300. The red line ε_{err} is an error estimate calculated using the unaligned horizontal terms.

Triple products in the Farfield (Fig. 11) are somewhat smaller and patchier than in the Nearfield. Smaller magnitudes are to be expected, because the product of mean variances appearing under the square root in the denominator of (19) was a factor of 5 smaller in the Farfield. Average ε_* is about 8.8×10^{-8} W kg^{-1} with a maximum of 1.9×10^{-7} W kg^{-1}. Unlike in the Nearfield, this maximum appears near the top of the profile. However, a second maximum, which is nearly as large, at 1.8×10^{-7} W kg^{-1}, appears near 430-m depth. Correlations were slightly higher than in the Nearfield, with an average r_* of 0.085. A strong patch of red interactions intermixed with blue can be seen at middepth after day 300. This burst of activity may be associated with an eddy that moved into the measurement area near the end of the deployment. An alternate average, indicated by the green line, was formed to assess the effect of the burst by using only data before day 300. The differences appear modest. ε_* decreased by about a third in a range of about 80 m above and below 430 m, and the local maximum dropped to 1.1×10^{-7} W kg^{-1} using the alternative averaging period. However, the maximum near the top of the profile increased to 2.3×10^{-7} W kg^{-1}.

4. Energy transfer bispectra

Although ε_* quantifies the net energy transfer between low- and high-frequency waves, bispectral methods (Hinich and Clay 1968; Kim and Powers 1979) identify

specific frequencies and wavenumbers of waves that are interacting. Bispectra have been used to examine nonlinear coupling in a variety of settings, including plasma flows (Kim and Powers 1979) surface gravity waves (Elgar and Guza 1985; Elgar et al. 1995), and internal waves (McComas and Briscoe 1980; Furue 2003; Furuichi et al. 2005; Carter and Gregg 2006; Frajka-Williams et al. 2006; Sun and Pinkel 2012, manuscript submitted to *J. Phys. Oceanogr.*).

Consider three random, real variables x, y, z with Fourier coefficients in frequency–wavenumber (ω, $\mathbf{k}$) space that are denoted by $X(\omega, \mathbf{k})$, $Y(\omega, \mathbf{k})$, $Z(\omega, \mathbf{k})$. The bispectrum of these variables is defined as

$$
\begin{aligned}
B(\omega_1, &\mathbf{k}_1, \omega_2, \mathbf{k}_2) \\
&= E \lfloor X(\omega_1, \mathbf{k}_1), Y(\omega_2, \mathbf{k}_2), Z(-\omega_1 - \omega_2, -\mathbf{k}_1 - \mathbf{k}_2) \rfloor, \\
&= E[X(\omega_1, \mathbf{k}_1), Y(\omega_2, \mathbf{k}_2), Z^*(\omega_1 + \omega_2, \mathbf{k}_1 + \mathbf{k}_2)],
\end{aligned}
$$
(21)

where $E[\cdot]$ indicates an expected value.

In three spatial dimensions, $\mathbf{k} = (k, l, m)$, the bispectrum is a function defined over an eight-dimensional space. Here we consider only vertical wavenumbers, so that four-dimensional bispectra are estimated. The analysis is further simplified if we consider bispectra of either wavenumber or frequency alone. Because the energetic shears in the observations are concentrated at low frequencies and we are primarily interested in

identifying up-frequency transfers, we begin by examining frequency bispectra. We define the frequency bispectrum over Fourier frequency pairs (ω_1, ω_2) as

$$B(\omega_1, \omega_2) = E[X(\omega_1), Y(\omega_2), Z^*(\omega_1 + \omega_2)]. \tag{22}$$

The magnitude of the bispectrum depends on both on the magnitudes and relative phases of the respective Fourier coefficients. The normalized bispectrum, also called the bicoherence, measures phase locking only. We use a normalization (McComas and Briscoe 1980; Elgar and Guza 1988; Hinich and Wolinsky 2005), which has a form consistent with (19), for the bicoherence,

$$b = \frac{|B(\omega_m, \omega_n)|}{\sqrt{E[|X(\omega_1)|^2]E[|Y(\omega_2)|^2]E[|Z^*(\omega_1 + \omega_1)|^2]}}. \tag{23}$$

Statistically significant phase locking is demonstrated when the sample bicoherence exceeds zero by an appropriate threshold, where thresholds for 90%, 95%, and 99% confidence at m degrees of freedom (DOF) are given by

$$b_{90\%} = \sqrt{4.6/m}, \quad b_{95\%} = \sqrt{6.0/m}, \quad \text{and}$$

$$b_{99\%} = \sqrt{9.2/m}, \tag{24}$$

respectively.

The direct relationship between the bispectrum (22) and ε_* can be shown by expressing the quantities u_j, w, and $\partial U_j/\partial z$ as Fourier series with N coefficients,

$$u_j'(t) = \sum_n \mathcal{U}_{j,n} e^{i\omega_n t}, \quad w'(t) = \sum_n \mathcal{W}_n e^{i\omega_n t},$$

$$\partial U_i/\partial z = \sum_n \mathcal{Z}_{j,n} e^{i\omega_n t}, \quad \omega_n = 2\pi n/N,$$

$$n = -\frac{N}{2}, \ldots, \frac{N}{2} - 1. \tag{25}$$

Then

$$u_j' w' \partial U_j/\partial z = \sum_m \mathcal{U}_{j,m} e^{i\omega_m t} \cdot \sum_n \mathcal{W}_n e^{i\omega_n t} \cdot \sum_p \mathcal{Z}_{j,p} e^{i\omega_p t} \tag{26}$$

$$= \sum_m \sum_n \sum_p \mathcal{U}_{j,m} \mathcal{W}_n \mathcal{Z}_{j,p} e^{i(\omega_m + \omega_n + \omega_p)t}. \tag{27}$$

Time averaging over the length of the Fourier transform causes all the exponential terms except those with zero frequency to vanish; thus,

$$\langle u_j' w' \partial U_j/\partial z \rangle = \sum_m \sum_n \sum_p \mathcal{U}_{j,m} \mathcal{W}_n \mathcal{Z}_{j,p} \delta(\omega_m + \omega_n + \omega_p), \tag{28}$$

$$= \sum_m \sum_n \mathcal{U}_{j,m} \mathcal{W}_n \mathcal{Z}_{j,-m-n}, \tag{29}$$

or equivalently

$$= \sum_m \sum_n \mathcal{U}_{j,m} \mathcal{W}_n \mathcal{Z}_{j,m+n}^*. \tag{30}$$

The expected values of the terms in the summation are exactly the bispectrum (22) between u_i, w, and $\partial U_i/\partial z$ at each (ω_m, ω_n). Their sum is a real-valued energy transfer, so that we can restrict one of m or n to positive values while keeping the summands real-valued by combining complex conjugates,

$$\sum_{m=-N/2}^{N/2-1} \sum_{n=-N/2}^{N/2-1} \mathcal{U}_{j,m} \mathcal{W}_n \mathcal{Z}_{j,m+n}^*$$

$$= \sum_{m=1}^{N/2-1} \sum_{n=-N/2}^{N/2-1} \mathcal{U}_{j,m} \mathcal{W}_n \mathcal{Z}_{j,m+n}^* + \mathcal{U}_{j,m}^* \mathcal{W}_n^* \mathcal{Z}_{j,m+n} \tag{31}$$

$$= \sum_{m=1}^{N/2-1} \sum_{n=-N/2}^{N/2-1} 2 \cdot \Re\{\mathcal{U}_{j,m} \mathcal{W}_n \mathcal{Z}_{j,m+n}^*\}. \tag{32}$$

We define the energy transfer bispectrum between u_i', w', and $\partial U_i/\partial z$ as the expected values of terms appearing in the sum, where we have included both horizontal directions and incorporated a sign change such that a positive energy transfer is from low to high frequency,

$$B_*(\omega_m, \omega_n) = E[-2 \cdot \Re\{\mathcal{U}_{1,m} \mathcal{W}_n \mathcal{Z}_{1,m+n}^* + \mathcal{U}_{2,m} \mathcal{W}_n \mathcal{Z}_{2,m+n}^*\}]. \tag{33}$$

By this definition,

$$\varepsilon_* = \sum_{m=1}^{N/2-1} \sum_{n=-N/2}^{N/2-1} B_*(\omega_m, \omega_n). \tag{34}$$

a. Frequency bispectra

The original depth–time records of u_i', w', and $\partial U_i/\partial z$, rather than the WKB-scaled versions, are used to form frequency bispectra. This allows direct comparison between energy transfer bispectra and the energy transfer rates ε_*, shown in Figs. 10 and 11, which are also computed using unscaled data. Time series from each Eulerian depth are Fourier transformed in nonoverlapping segments of length 1024, or about 68.3 h. A 5% Tukey taper is applied to each segment. Separate bispectral realizations are formed for each depth–time segment between 100 and 700 m depth. The realizations, excluding the contaminated sonar depths, are then averaged together to form sample estimates for the bispectrum and bicoherence. Both B_* and the squared bicoherence b^2 are smoothed with a 3×3 bin moving average, which spans an approximately 1 cpd $\times$ 1 cpd region. The resulting bispectral densities are presented in Figs. 12 and 13. Each value $B_*(\omega_u, \omega_w)$ is plotted on
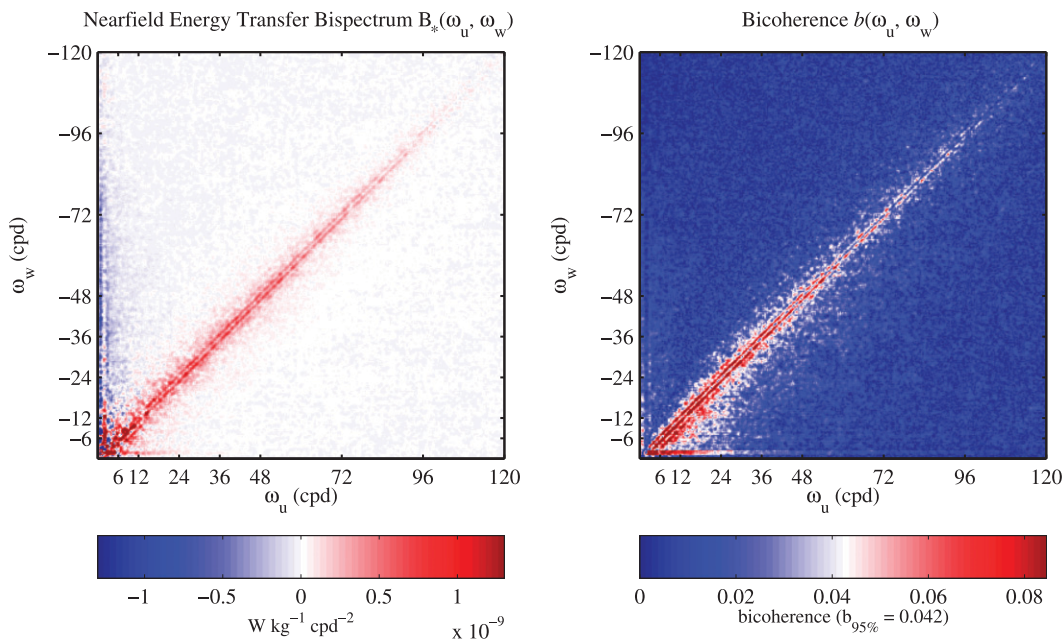
FIG. 12. Nearfield: energy transfer bispectral estimates. (left) Energy transfer bispectrum $B_*(\omega_u, \omega_w)$: bispectral densities plotted at coordinates (ω_u, ω_w) correspond to triads $(\omega_u, \omega_w, -\omega_u, -\omega_w)$. Most of the positive energy transfers (red) are concentrated near the diagonal line $\omega_u = -\omega_w$, but some negative energy transfers (blue) are seen at low frequencies as well. (right) Bicoherence $b(\omega_u, \omega_w)$: the color scale is adjusted so that white and red represent statistically significant values larger than $b_{95\%} = 0.019$.

the bifrequency plane at the coordinates (ω_u, ω_w). Following the indexing convention in the summation (33), the horizontal axis is restricted to positive frequencies ω_u, whereas frequencies ω_w on the vertical axis are signed to account for both sum and difference interactions. The third frequency, which is associated with the Fourier coefficients of the shears $(\partial U_i / \partial z)$, is always the negative sum of the coordinates, $(\omega = -\omega_u - \omega_w)$. It will sometimes be useful in the discussion to indicate the third frequency explicitly. For example, the bispectral density plotted at the coordinates $(16, -17)$ cpd is referred to explicitly as $B_*(16, -17, 1)$ cpd. No significant bispectral values are found in the lower half plane, where interactions would involve ω_u and ω_w with the same signs and a high-frequency shear, so only the upper half plane is shown in the figures.

Positive energy transfers, shown in red in the energy transfer bispectra, are spread along the diagonal $\omega_w = -\omega_u$ in both Figs. 12 and 13, suggesting that pairs of high-frequency waves are interacting with and receiving energy from shears with close to zero frequency. Negative energy transfers, colored blue, also appear in both figures near the vertical axis $\omega_u = 0$. In addition, a pair of positive ridges is seen only the Nearfield bispectrum (Fig. 12) near $\omega_u = 2$ cpd, $\omega_w = -2$ cpd and may be associated with PSI energy transfers.

From (24) we estimate a 95% confidence threshold for zero bicoherence of $b_{95\%} = 0.042$ in the Nearfield and $b_{95\%} = 0.044$ in the Farfield. The color scale for the bicoherence plots is chosen so that values at the threshold appear in white, with larger values tending toward red. In estimating the effective degrees of freedom in the bicoherence estimate, we regard measurements separated by 50 m, or approximately half a near-inertial wavelength, as independent. This results in 186 independent realizations for each of two horizontal directions in the Nearfield and 174 realizations in the Farfield. Both estimates are improved by a factor of 9 by the 3×3 smoothing in bifrequency space.

The significant bicoherence in Figs. 12 and 13 is, like the positive bispectra, concentrated along the diagonal $(\omega_w = -\omega_u)$. However, unlike the bispectra, the bicoherence appears in a band that widens with increasing frequency. Notably, bicoherences are also spread at isolated points throughout the bifrequency plane, especially at frequencies above 48 cpd in Fig. 13. The increasing spread of bicoherences at high frequencies may be due to Doppler shifting or measurement noise that has contaminated the Fourier coefficients. Fortunately, the noise seems to appear mostly where the bispectra are small, so that the energy transfer estimates are relatively unaffected.
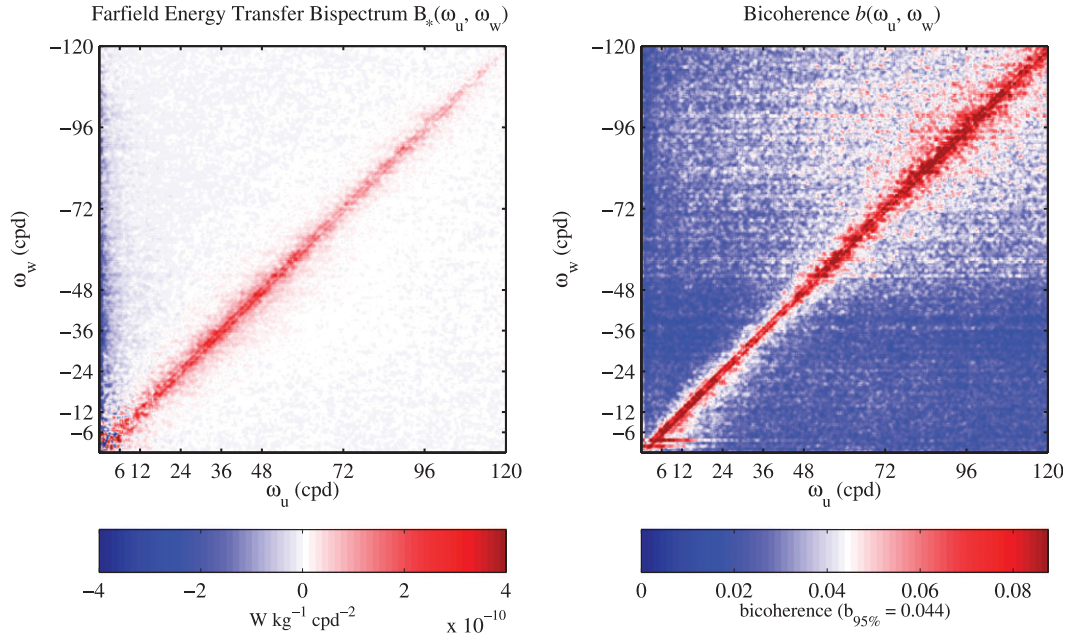
FIG. 13. Farfield: energy transfer bispectral estimates. As in Fig. 12, but for the Farfield. (left) Energy transfer bispectrum $B_*(\omega_u, \omega_w)$: bispectral densities plotted at coordinates (ω_u, ω_w) correspond to triads $(\omega_u, \omega_w, -\omega_u, -\omega_w)$. Most of the positive energy transfers (red) are concentrated near the diagonal line $\omega_u = \omega_w$, but again some negative energy transfers (blue) are seen at low frequencies. (right) Bicoherence $b(\omega_u, \omega_w)$: the color scale is adjusted so that white and red represent statistically significant values larger than $b_{95\%} = 0.020$.

The bispectral energy transfers and bicoherence thresholds are combined in the bispectral plots of Figs. 14 and 15. Here, $B_*(\omega_u, \omega_w)$ has been masked to show only significantly bicoherent energy transfers. Most of the positive energy transfers near the diagonal remain intact, whereas the negative energy transfers near $\omega_u = 0$ have been removed. A small remnant of the ridge along $\omega_w = -2$ cpd also remains in Fig. 14.

The energy transfers near $(\omega_w = -\omega_u)$ do not lie directly on the diagonal itself but rather along a pair of slightly offset ridges. A detailed view of this feature is provided in the inset in each figure. Guide lines drawn along constant sum frequencies $\omega_u + \omega_w = \pm f$, indicate where interactions between two high-frequency waves and a pure inertial wave (frequency $\pm f$) would lie in the plot.

Below the bispectra in Figs. 14 and 15 are plots showing net energy transfer due to high-frequency waves up to and including the frequency ω,

$$\int_{6\,\mathrm{cpd}}^{\omega} \int_{6\,\mathrm{cpd}}^{\omega} B_*(\omega_u, \omega_w)\, d\omega_w\, d\omega_u. \qquad (35)$$

The integration begins at $\omega_u = 6$ cpd to be consistent with ε_*, which was calculated with a gap between 3 and 6 cpd. The ridge in the Nearfield at $\omega_w = -2$ cpd falls within the gap and is thus omitted from the integral.

There is a falloff in energy transfer with increasing frequency beginning at about 72 cpd, with very little contribution from frequencies above 96 cpd, which exceeds $N(z)$ at most depths. In the Nearfield, B_* approaches 2.8×10^{-7} W kg^{-1}. The Farfield value is 1.2×10^{-7} W kg^{-1}. The estimates of energy transfer formed by integrating the bispectra are in close agreement with the depth-averaged values of ε_* (Figs. 10, 11).

b. Wavenumber bispectra

Although the significant bicoherences in both the Nearfield and the Farfield imply that interactions are occurring between the energetic low-frequency shears and a variety of high-frequency waves, the frequency analysis gives insufficient information for determining whether the interactions resemble ID, ES, or neither. It should be possible to distinguish between the high-frequency members in ID (similar vertical wavenumbers that are much larger than the low-frequency shear wavenumbers) and ES (similar but opposite-signed wavenumbers that are smaller than the shear wavenumbers).

A similar procedure as used in the frequency analysis can be used to form vertical wavenumber bispectra. WKB-scaled and WKB-stretched quantities are used for the wavenumber analysis to minimize effects from wave refraction. Although before B_* was defined over bifrequencies (ω_u, ω_w), here we define $B_*(\kappa_u, \kappa_w)$ over

Nearfield Energy Transfer Bispectrum B$_*$(ω_u, ω_w) for | b | > $b_{95\%}$

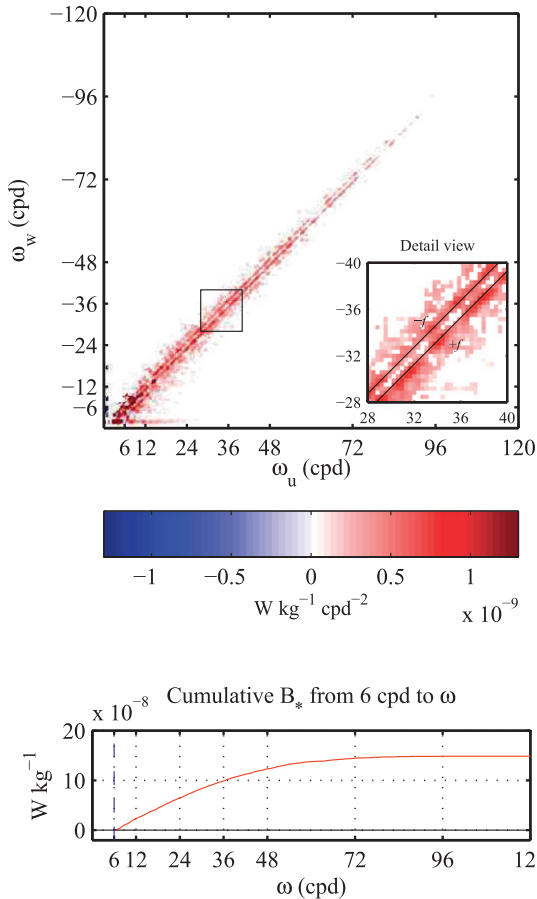Farfield Energy Transfer Bispectrum B$_*$(ω_u, ω_w) for | b | > $b_{95\%}$

FIG. 14. Nearfield: energy transfer bispectrum $B_*(\omega_u, \omega_w)$. As in Fig. 12, but showing only bicoherent energy transfers. (top) A detailed view inset shows that the sum frequencies of triads near the diagonal are not precisely zero but differ by about f. (bottom) A plot shows of the cumulative integral of energy transfer rate with frequency.
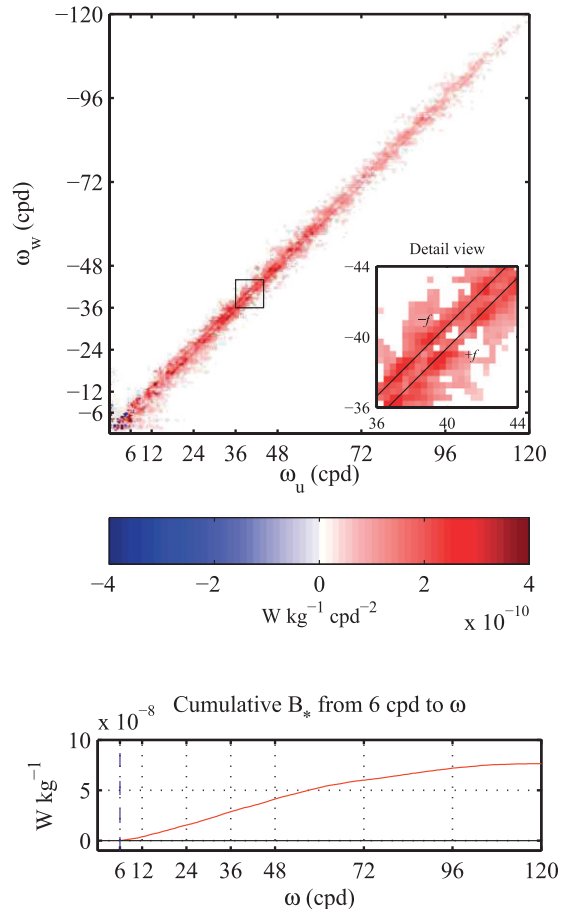
FIG. 15. Farfield: energy transfer bispectrum $B_*(\omega_u, \omega_w)$. As in Fig. 13, but showing only bicoherent energy transfers. (top) A detailed view inset shows that the sum frequencies of triads near the diagonal are not precisely zero but differ by about f. (bottom) A plot shows of the cumulative integral of energy transfer rate with frequency.

vertical wavenumber pairs. Prior to Fourier transforming in wavenumber, the frequency separation between low- and high-frequency fields is ensured by bandpass filtering in the time domain, as was done in estimating ε_*. The data are then windowed using a 5% Tukey taper in depth. Only profiles 500–7499 are used from each dataset. This particular span is chosen for three reasons: to allow time for the low-pass filter output to stabilize after the beginning of the record, to avoid the interruption around day 8099 in the Nearfield, and to exclude the eddy-associated activity after day 300 in the Farfield. The number of profiles used from each site is kept the same to simplify statistical comparison.

Vertical wavenumber bispectral estimates from the Nearfield and Farfield are presented in Figs. 16 and 17. Although only difference reactions are possible in the

bifrequency plane because of the frequency gap between low- and high-frequency waves, no similar restriction has been placed upon the interacting wavenumbers. Both sum and difference interactions (κ_w both positive and negative) are found to be important, and thus both half planes are shown. The bispectral smoothing window, formed by convolving a 2 × 2 bin square filter with itself, has been chosen because it has the same effective width as the 2 × 2 bin square filter but is symmetric around its center.

Nearfield energy transfers, shown in the left panel of Fig. 16, are confined in a small region of biwavenumber space that corresponds to small vertical wavenumbers (κ_u, κ_w). In the Farfield (Fig. 17), the region is significantly elongated in the horizontal direction but remains close to the horizontal κ_u axis. Bicoherence thresholds

Nearfield Bispectrum B$_*$(κ_u, κ_w)   Bicoherence b (κ_u, κ_w)   B$_*$(κ_u, κ_w) for $b > b_{95\%}$
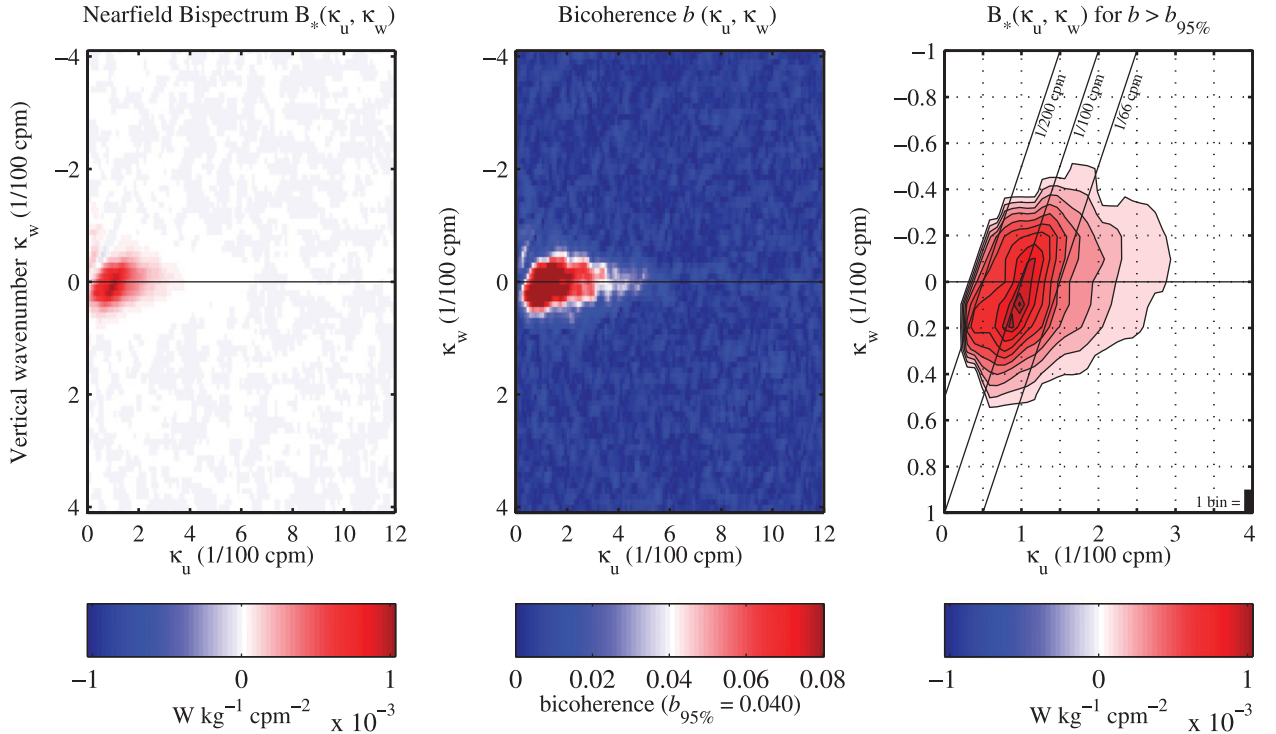

FIG. 16. Nearfield: wavenumber bispectral estimates. (left) Wavenumber bispectrum $B_*(\kappa_u, \kappa_w)$: nearly all the energy transfers are concentrated at very low wavenumbers. (middle) Bicoherence $b(\omega_u, \omega_w)$: the energy transfers appear to be bicoherent. Possible noise at high frequencies, not associated with significant energy transfers, is apparent. (right) $B_*(\kappa_u, \kappa_w, -\kappa_u, -\kappa_w)$ showing bicoherent values only: a contour plot is used to help locate the peak wavenumbers. Guide lines indicate constant sum wavenumbers $(-\kappa_u, -\kappa_w)$.

computed according to (24) are shown in the second panel of each figure. Profiles separated in time by 2 h, or a half period of the 6-cpd cutoff for the high-frequency band, are taken as independent measurements. In both HOME locations, the bicoherent regions contain the regions with the largest energy transfer but also extend in a band along the κ_u axis toward high wavenumber.

The rightmost panel of each figure shows a contour plot of the low-wavenumber region that contains the bicoherent energy transfers. A black tile indicates the size of each (κ_u, κ_w) bin. Individual peaks are best seen in the contour plots. The strongest peak in the Nearfield is at on the sum interaction side, seen in Fig. 16 at $(\kappa_w, \kappa_u, -\kappa_w - \kappa_u) \approx (0.9, 0.2, -1.1) \times 10^{-2}$ cpm, and involving high-frequency waves with a vertical wavenumber ratio $\kappa_u/\kappa_w \approx 4.5/1$, which is far from the approximately equal wavenumbers expected for either ID or ES. A second peak at $(0.4, 0.2, -0.6) \times 10^{-2}$ cpm has somewhat less disparate ratio of about $^2/_1$. However, the narrower peak at $(1.2, -0.2, -1.0) \times 10^{-2}$ cpm is even further from unity, at about $^6/_1$. In the main interactions seen here, κ_w is consistently in the second lowest wavenumber bin, which corresponds to a wavelength on the order of 500 m.

In the Farfield, the high-frequency vertical wavenumbers tend to be even more widely disparate. Figure 17 shows a set of major peaks corresponding to sum interactions between waves at $\kappa_w = 0.15 \times 10^{-2}$ cpm and waves at $\kappa_u = 1.5, 0.6,$ and 1.0×10^{-2} cpm, where the frequencies are listed in descending strength of the interactions. On the difference side, waves with similarly long wavelength, at $\kappa_w = -0.15 \times 10^{-2}$ cpm, interact with waves at $\kappa_u = 1.9, 0.8,$ and 1.5×10^{-2} cpm. The peaks appear to be in pairs that have their third wavenumbers $(-\kappa_u - \kappa_w)$ in common.

c. Wavenumber–frequency slices

It is possible to include incorporate some useful frequency information in the wavenumber analysis without resorting to full wavenumber–frequency bispectra. We do so by bandpass filtering the high-frequency waves into one-octave ranges: 6–12 cpd, 12–24 cpd, 24–48 cpd, and 48–96 cpd, using sixth-order Butterworth filters throughout. Because nearly all the energy transfers seen in Figs. 14 and 15 are concentrated near the diagonal, we compute a series of wavenumber bispectra, each using u' and w' from a single frequency range. As before, the low-frequency waves include frequencies up to 3 cpd.
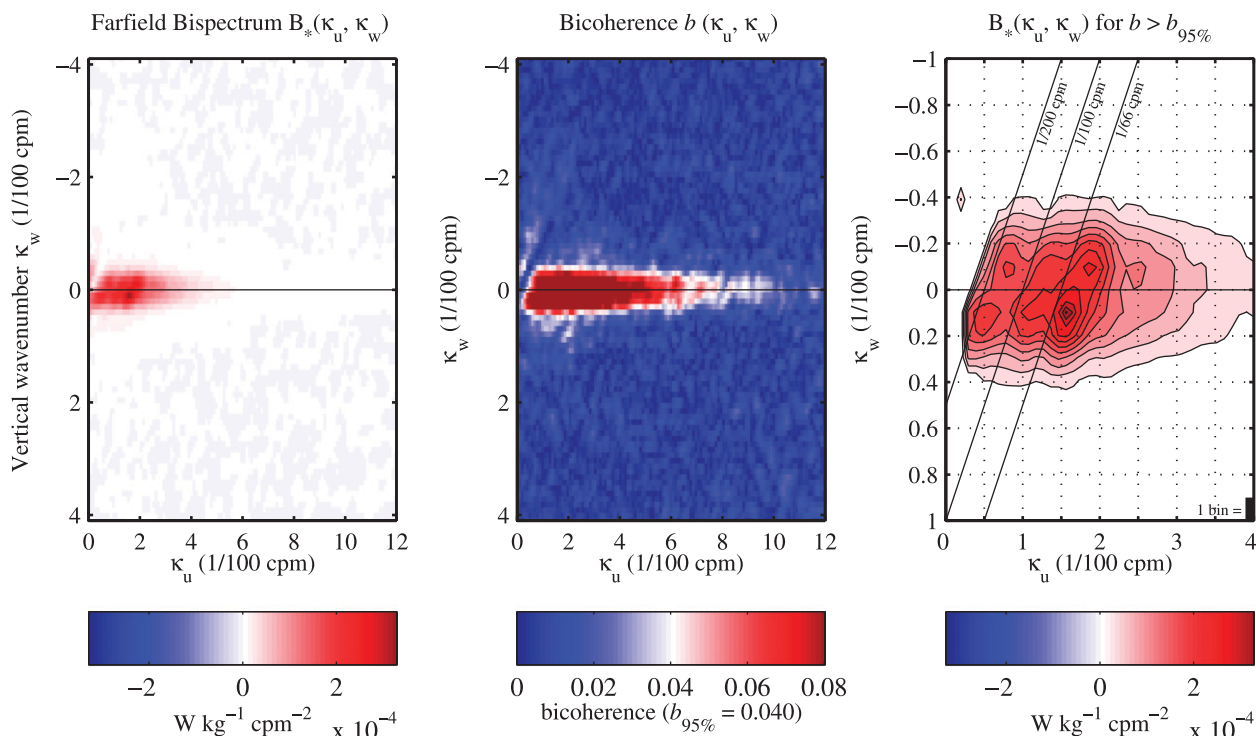
FIG. 17. Farfield: wavenumber bispectral estimates. As in Fig. 16, but for the Farfield. (left) Wavenumber bispectrum $B_*(\kappa_u, \kappa_w)$: the energy transfers are concentrated at very low wavenumbers, but the active region is elongated along the κ_u axis. (middle) Bicoherence $b(\omega_u, \omega_w)$: a wide band extending along the κ_u axis to high wavenumbers is above the bicoherence threshold. (Right) $B_*(\kappa_u, \kappa_u, -\kappa_u - \kappa_w)$ showing bicoherent values only: a contour plot is used to help locate the peak wavenumbers. Guide lines indicate constant sum wavenumbers $(-\kappa_u - \kappa_w)$.

Figures 18 and 19 show the resulting wavenumber–frequency slices. Bicoherence thresholding has already been applied as in the rightmost panels of Figs. 16 and 17. As can be anticipated from the cumulative integrals of energy transfer in Figs. 14 and 15, the strongest energy transfers involve waves in the 24–48-cpd frequency range. Some of the interactions can be partially localized in frequency: for example, in the Nearfield the $(0.9, 0.2, -1.1) \times 10^{-2}$ cpm peak is seen strongly in the 24–48-cpd slice and less so in the 48–96-cpd slice, whereas the $(0.4, 0.2, -0.6) \times 10^{-2}$ cpm interaction seems to be found mostly in the 6–12- and 12–24-cpd slices. In the Farfield, however, most of the peaks appear in much the same locations regardless of frequency.

d. The interacting triads

Based on the bispectral analysis, we can form a general picture of the wave triads involved in the observed energy transfers. The triangles in Fig. 20 depict example sum and difference triads in which the wave vectors, $\mathbf{k} = (k, \kappa)$, $\mathbf{k}_1 = (k_1, \kappa_1)$, $\mathbf{k}_2 = (k_2, \kappa_2)$, are coplanar.

If we assume linear dispersion (3), then the aspect ratio k/κ of each wave is determined by its frequency,

$$\frac{k}{\kappa} = \left(\frac{\omega^2 - f^2}{N^2 - \omega^2} \right)^{1/2}. \qquad (36)$$

The lowest frequency in the triad is $\omega \approx f$, so that the wave vector $\mathbf{k}$ is nearly vertical. The sides $\mathbf{k}_1$, $\mathbf{k}_2$ correspond to waves at higher frequencies $(\omega_1, \omega_2) \approx (\omega_1, \omega_2 + f)$.

As seen from the frequency bispectra (e.g., Fig. 14), a typical value for ω_1 might be 24 cpd. Using values from the Nearfield of $f = 0.74$ cpd, $N \approx 100$ cpd, we find that $(\omega_1, \omega_2) \approx (32f, 33f)$.

Because $k \approx 0$, the remaining sides have approximately equal horizontal wavenumber $k_H = k_1 \approx k_2$. We can estimate the relationship κ_1/κ_2 between their vertical wavenumbers using (36),

$$\kappa_1/\kappa_2 \approx (k_2/\kappa_2)/(k_1/\kappa_1) \quad \text{and} \qquad (37)$$

$$= \left(\frac{\omega_2^2 - f^2}{N^2 - \omega_2^2} \right) \Big/ \left(\frac{\omega_1^2 - f^2}{N^2 - \omega_1^2} \right). \qquad (38)$$

For frequencies $(32f, 33f)$ we find $\kappa_1/\kappa_2 \approx 1.04$, meaning that the vertical wavenumbers are nearly indistinguishable
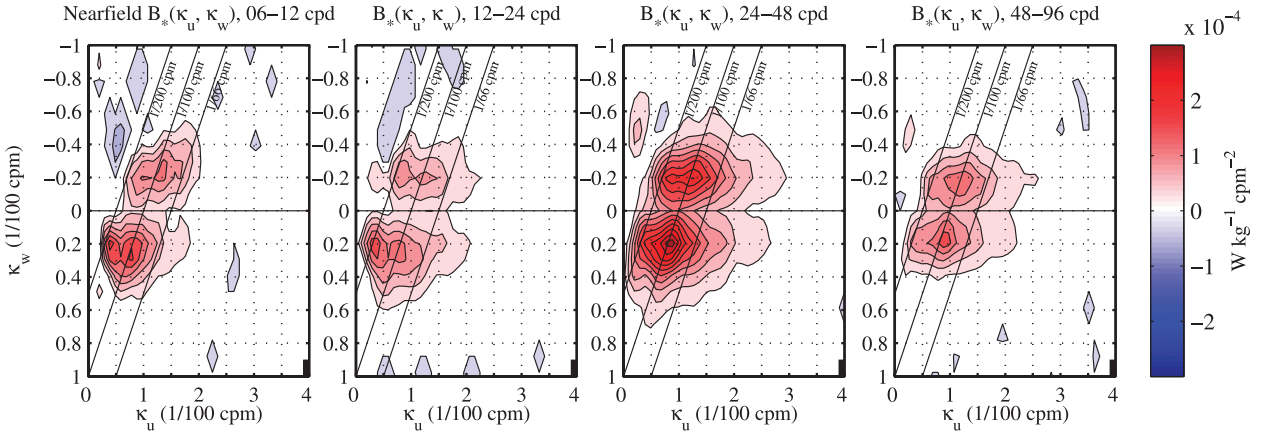
FIG. 18. Nearfield: wavenumber–frequency bispectral slices. As in Fig. 16, but calculated for a series of frequency slices that include only high-frequency waves in the bands 6–12 cpd, 12–24 cpd, 24–48 cpd, and 48–96 cpd. Some bispectral peaks appear to be localized in frequency, but there appears to be significant leakage across slices.

from each other. In the sum reaction, the triangle is nearly isosceles, and we recognize the elastic scattering triad. The difference reaction is induced diffusion. In the wavenumber bispectra, however, we find relatively large ratios of $\kappa_2/\kappa_1 > 2$, which suggests that we are far from the limiting cases of McComas and Bretherton (1977).

If resonant ID triads involve a pair of high-frequency waves that differ only slightly in wavenumber, and ES triads involve a pair of high-frequency waves that are vertical near reflections of one another, then the interactions found here resemble neither case. Nor is it clear that eikonal models of ID provide a useful explanation for the observed ε_*, because the waves we find interacting are not small-scale packets propagating through large-scale background shears but are even larger–scale waves for which the shears do not represent a slowly varying background in a ray-tracing sense.

One possibility for reconciling the observed frequencies $\omega \gg f$ with the large differences in aspect ratios is that the high-frequency waves are actually waves that have been Doppler shifted from low frequencies very close to f, where a small change in frequency can lead to a large change in aspect ratio. For example, one particular triad of frequencies that is familiar from studies of parametric subharmonic instability, $(\omega, \omega_1, \omega_2) = (f, M_2 - f, M_2)$, has a ratio $\kappa_1/\kappa_2 = 1.9$. If the lowest frequency in the triad is superinertial, then somewhat higher ratios are possible: for example, $(1.2f, M_2 - 1.2f, M_2)$, gives a ratio $\kappa_1/\kappa_2 = 2.5$. However, we estimate that a flow on the order of 3 m s^{-1} would be required to Doppler shift the $(f, M_2 - f, M_2)$ triad so that the M_2 wave is encountered at 24 cpd, where the inertial wave has vertical wavenumber on the order of $^1/_{100}$ cpm. Details of the calculation are found in the appendix. Given
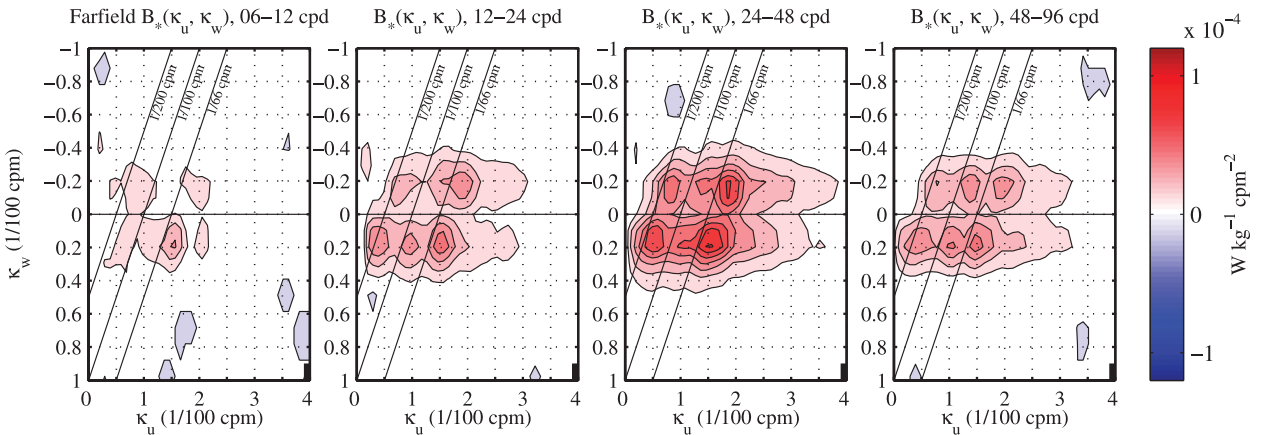

FIG. 19. Farfield: wavenumber–frequency bispectral slices. As in Fig. 17, but calculated for a series of frequency slices that include only high-frequency waves in the bands 6–12 cpd, 12–24 cpd, 24–48 cpd, and 48–96 cpd. In general, the bispectral peaks in the Farfield do not appear to be well localized in frequency.
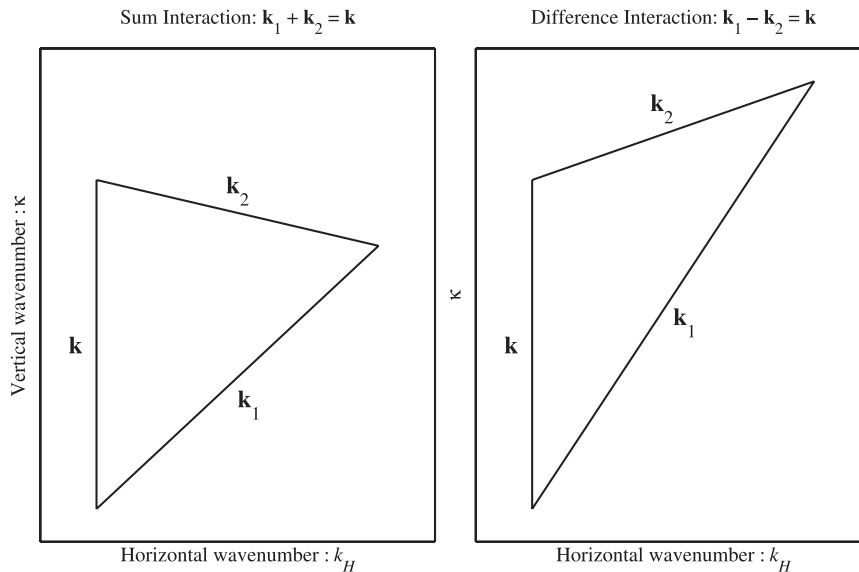
FIG. 20. Sum and difference triads. Example triads are diagrammed in vertical κ and horizontal k_H wavenumber space. In each case, $\mathbf{k}$ is the near-inertial ($\omega \approx f$) member of the triad and thus has a nearly vertical wave vector.

that barotropic flows in the Nearfield were on the order of 30 cm s^{-1}, Doppler shifting of very low-frequency waves to high encounter frequencies seems unlikely to explain the triads we observe.

Because (36) is symmetric with respect to f and N, another possibility is that the high-frequency waves have intrinsic frequencies very close to N. For example, $\kappa_1/\kappa_2 = 2.1$ for a triad with the same inertial wavenumber as before and frequencies (f, $N - 1.3f$, $N - 0.3f$). In the bottom 200 m of the Nearfield profiles, N ranges from about 37 to 67 cpd, so that waves with frequency near N would be detected as high-frequency waves even with very little Doppler shifting downward in frequency. However, this explanation would require that most of the interactions involve waves close to the high-frequency limit for internal waves. An additional difficulty is that N increases with height, so that upward-propagating waves that are near N at a given depth would quickly find themselves far from N. In general, the validity of the weakly resonant theory is unclear for waves propagating through significant changes in N within fractions of a wavelength.

e. The energy transfer rate ε_* and turbulent dissipation ε

High-frequency internal waves are known eventually to break, resulting in turbulent mixing (Alford and Pinkel 2000a). How important are the observed energy transfers to the high-frequency energy balance? To answer this question, we compare ε_* to independent estimates of the turbulent dissipation rate ε.

Dissipation measurements were made at several sites in HOME Nearfield using a combination of tethered profilers and towed instruments. Directly over the ridge, Klymak et al. (2006) reported averaged diffusivities on top of the ridge of $K_\rho \approx 10^{-4}$ m^2 s^{-1} near the surface to 5×10^{-3} m^2 s^{-1} near the bottom. These values correspond, through the Osborn (1980) relationship,

$$K_\rho = \Gamma \frac{\varepsilon_*}{\langle N^2 \rangle}, \tag{39}$$

to dissipations of $\varepsilon = 8 \times 10^{-8}$ W kg^{-1} and 2×10^{-7} W kg^{-1}, using nominal values $N = 180$ and 47 cpd, respectively. An analysis by Klymak et al. (2008) of data collected aboard *FLIP* during HOME Nearfield found similar values for ε at the mooring site.

The apparent agreement in magnitude between ε_* and ε suggests that the interactions found here may be of first-order importance to the energy balance between internal waves and dissipation. On the other hand, much of the deep turbulent mixing in the Nearfield has been attributed to unrelated processes such as direct breaking of the internal tide near the sloping bottom (Klymak et al. 2008), but agreement in the upper ocean is promising.

5. Summary

We report energy transfers from low-frequency, high-shear internal waves to high-frequency waves in two sites near Hawaii, using stress–shear triple correlations. The internal wave field at the HOME Nearfield location

is characterized by elevated tidal amplitudes and shear variance relative to open-ocean levels. Velocity spectra are dominated by the semidiurnal tide and a set of peaks at possible tidal harmonics, mostly associated with upward-propagating wave energy. The HOME Farfield wave field is somewhat less energetic and displays neither a marked vertical asymmetry nor prominent spectral peaks other than at near-inertial and semidiurnal frequencies.

The energy transfer rate ε_* in the Nearfield is approximately 1.8×10^{-7} W kg^{-1}, averaged from 100- to 700-m depths. In the Farfield, where the variances of the correlated terms are 5 times smaller, averaged ε_* is about a factor of 2 smaller, at 8.8×10^{-8} W kg^{-1}. Correlation coefficients r_* are similar at 0.075 in the Nearfield and 0.085 in the Farfield. Nearfield energy transfers are largest in the lower part of the profiling column where both shear and tidal amplitudes are large, whereas ε_* is large in the Farfield near the surface.

Bispectral analysis demonstrates significantly bicoherent interactions between low-frequency waves and a broad range of higher-frequency waves with similar frequencies. Wavenumber bispectra find that the low-frequency wave in each triad tends to have a wavelength on the order of 100 m, as does one of the high-frequency waves. However, the other high-frequency wave has a much longer wavelength. The large mismatch between the aspect ratios of the high-frequency waves is contrary to classical definitions of induced diffusion or elastic scattering interactions. Doppler shifting of the higher-frequency waves in each triad from either very low frequencies or very high frequencies does not appear to explain the anomalous aspect ratios. The horizontal velocities required to shift waves with intrinsic frequencies near f to observed frequencies of 24 cpd or higher are an order of magnitude too large for tidal velocities, even in the Nearfield.

Observed energy transfers in the Nearfield have similar magnitude to measurements of turbulent dissipation near Kaena Ridge. The implication is that the interaction may be a significant step in the energy cascade from low frequencies and scales near 100 m to breaking waves and mixing. Although other pathways were seen in HOME, including the direct breaking of near-seafloor bores (Levine and Boyd 2006; Aucan et al. 2006; Klymak et al. 2008) and the breaking of high-mode D_2 lee waves (Klymak et al. 2010), we feel that this pathway remains active in the open ocean, as suggested by the finding of a similar interaction in the Farfield, far from the ridge slope.

Further study of the interaction is warranted. The mismatch between the observed triads and the resonance condition is troubling, yet the energy transfer rates appear robust. Why is this particular interaction detectable relative to the classical wave–mean shear exchange? Which of the high-frequency waves is the principal recipient of the energy? Which is the most likely to subsequently break?

APPENDIX

Doppler Shifting and Resonant Triads

The frequency at which we encounter (measure) a given wave that is being advected in a flow will differ from its intrinsic frequency, which is the frequency we would measure if there were no motion (or, equivalently, if we were moving with the flow). The frequency ω that we measure in an Eulerian frame can be related ω to the intrinsic frequency $\hat{\omega}$ and the flow velocity $\mathbf{u}$ through

$$\omega = \hat{\omega} + (\mathbf{k} \cdot \mathbf{u}). \qquad (A1)$$

The Doppler shift $(\mathbf{k} \cdot \mathbf{u})$ is due to the advection of spatial phase variations $\mathbf{k}$ past the fixed observer by the flow $\mathbf{u}$.

The resonance conditions (1) require that a resonant triad maintain fixed mutual phase in both space and time, so Doppler shifting by an external velocity field is not expected to affect the existence of resonant energy transfers, as all three waves will be advected in unison. However, waves can be shifted out of a given frequency band in which we had expected to find them. For example, the wavenumber–frequency shear spectra of shears (Figs. 5, 6) show the effects of Doppler shifting as K-shaped patterns that originate at low frequency and widen with increasing wavenumber. As discussed by Pinkel (2008), this is spreading of variance is partially due (tidal) vertical heaving of high-vertical-wavenumber shears. As a result, some of the low-frequency shear variance is encountered at high frequencies and falls outside our filter band for low-frequency ($\partial U / \partial_z$). The weighting of the spectrum toward low frequencies suggests that more variance is Doppler shifted out of the low-frequency band than is been shifted in from other frequencies.

Doppler shifts by vertical heaving cannot explain the observed frequencies of the triads. The near-inertial (observed) waves in each triad tend to have the largest vertical wavenumbers and would be easily Doppler shifted out of the low-frequency band by vertical motions. Consider instead Doppler shifting of the triad discussed above by a horizontal flow $\mathbf{u} = u$ such as the barotropic tide. The near-inertial member of the triad, with nearly zero horizontal wavenumber $k \approx 0$, is relatively unaffected by the horizontal flow. The other two members of the triad, sharing the same horizontal wavenumber k_h, are Doppler shifted by equal amounts.

How strong of a flow is needed to Doppler-shift the M_2 wave in the $(f, M_2 - f, M_2)$ triad to an observed frequency of 24 cpd? From Fig. 16, we can estimate a vertical wavenumber of $\kappa = 1/100$ cpm for the inertial wave.

Using $\kappa_1/\kappa_2 = 1.9$ and (36), we find a shared horizontal wavenumber for the $M_2 - f$, M_2 waves of $k_H = 7.7 \times 10^{-5}$ cpm. Then, using (A1),

$$24 \, \text{cpd} = M_2 + k_H u,$$

$$2.78 \times 10^{-4} \, \text{s}^{-1} \approx 2.2 \times 10^{-5} \, \text{s}^{-1} + (7.7 \times 10^{-5} \, \text{m}^{-1})u,$$

and

$$u \approx 3.3 \, \text{m s}^{-1}.$$

REFERENCES

Alford, M., and R. Pinkel, 2000a: Observations of overturning in the thermocline: The context of ocean mixing. *J. Phys. Oceanogr.,* **30,** 805–832.

——, and ——, 2000b: Patterns of turbulent and double-diffusive phenomena: Observations from a rapid-profiling micro-conductivity probe. *J. Phys. Oceanogr.,* **30,** 833–854.

——, and M. C. Gregg, 2001: Near-inertial mixing: Modulation of shear, strain and microstructure at low latitude. *J. Geophys. Res.,* **106** (C8), 16 947–16 968.

Aucan, J., M. A. Merrifield, D. S. Luther, and P. Flament, 2006: Tidal mixing events on the deep flanks of Kaena Ridge, Hawaii. *J. Phys. Oceanogr.,* **36,** 1202–1219.

Benney, D., and P. Saffman, 1966: Nonlinear interactions of random waves in a dispersive medium. *Proc. Roy. Soc. London,* **289A,** 301–320.

Broutman, D., and W. Young, 1986: On the interaction of small-scale oceanic internal waves with near-inertial waves. *J. Fluid Mech.,* **166,** 341–358.

Carter, G., and M. Gregg, 2006: Persistent near-diurnal internal waves observed above a site of M_2 barotropic-to-baroclinic conversion. *J. Phys. Oceanogr.,* **36,** 1136–1147.

Duda, T., and D. Jacobs, 1998: Stress/shear correlation: Internal wave/wave interaction and energy flux in the upper ocean. *Geophys. Res. Lett.,* **25,** 1919–1922.

Elgar, S., and R. Guza, 1985: Shoaling gravity waves: Comparisons between field observations, linear theory, and a nonlinear model. *J. Fluid Mech.,* **158,** 47–70.

——, and ——, 1988: Statistics of bicoherence. *IEEE Trans. Acoust. Speech Signal Process.,* **36,** 1667–1668.

——, T. Herbers, V. Chandran, and R. Guza, 1995: Higher-order spectral-analysis of nonlinear ocean surface gravity-waves. *J. Geophys. Res.,* **100** (C3), 4977–4983.

Frajka-Williams, E. E., E. L. Kunze, and J. A. MacKinnon, 2006: Bispectra of internal tides and parametric subharmonic instability. M.S. thesis, School of Oceanography, University of Washington, 26 pp.

Furue, R., 2003: Energy transfer within the small-scale oceanic internal wave spectrum. *J. Phys. Oceanogr.,* **33,** 267–282.

Furuichi, N., T. Hibiya, and Y. Niwa, 2005: Bispectral analysis of energy transfer within the two-dimensional oceanic internal wave field. *J. Phys. Oceanogr.,* **35,** 2104–2109.

Gargett, A., and G. Holloway, 1984: Dissipation and diffusion by internal wave breaking. *J. Mar. Res.,* **42,** 15–27.

Gill, A. E., 1982: *Atmosphere–Ocean Dynamics.* Academic Press, 662 pp.

Gregg, M. C., 1989: Scaling turbulent dissipation in the thermocline. *J. Geophys. Res.,* **94** (C7), 9686–9698.

Hasselmann, K., 1962: On the non-linear energy transfer in a gravity-wave spectrum. 1. General theory. *J. Fluid Mech.,* **12,** 481–500.

Henyey, F., and N. Pomphrey, 1983: Eikonal description of internal wave interactions—A non-diffusive picture of induced diffusion. *Dyn. Atmos. Oceans,* **7,** 189–219.

——, J. Wright, and S. Flatté, 1986: Energy and action flow through the internal wave field: An eikonal approach. *J. Geophys. Res.,* **91** (C7), 8487–8495.

Hinich, M., and C. Clay, 1968: The application of the discrete fourier transform in the estimation of power spectra, coherence, and bispectra of geophysical data. *Rev. Geophys. Space Phys.,* **6,** 289–346.

——, and M. Wolinsky, 2005: Normalizing bispectra. *J. Stat. Plann. Inference,* **130** (1–2), 405–411.

Jacobs, D. C., and C. S. Cox, 1987: Internal wave stress-shear correlations: A choice of reference frames. *Geophys. Res. Lett.,* **14** (1), 25–28.

Kim, Y., and E. Powers, 1979: Digital bispectral analysis and its applications to non-linear wave interactions. *IEEE Trans. Plasma Sci.,* **7,** 120–131.

Klymak, J. M., and Coauthors, 2006: An estimate of tidal energy lost to turbulence at the Hawaiian Ridge. *J. Phys. Oceanogr.,* **36,** 1148–1164.

——, R. Pinkel, and L. Rainville, 2008: Direct breaking of the internal tide near topography: Kaena Ridge, Hawaii. *J. Phys. Oceanogr.,* **38,** 380–399.

——, S. M. Legg, and R. Pinkel, 2010: High-mode stationary waves in stratified flow over large obstacles. *J. Fluid Mech.,* **644,** 321–366.

Levine, M. D., and T. J. Boyd, 2006: Tidally forced internal waves and overturns observed on a slope: Results from HOME. *J. Phys. Oceanogr.,* **36,** 1184–1201.

McComas, C. H., and F. Bretherton, 1977: Resonant interaction of oceanic internal waves. *J. Geophys. Res.,* **82** (9), 1397–1412.

——, and M. Briscoe, 1980: Bispectra of internal waves. *J. Fluid Mech.,* **97,** 205–213.

——, and P. Müller, 1981: The dynamic balance of internal waves. *J. Phys. Oceanogr.,* **11,** 970–986.

Müller, P., G. Holloway, and F. Henyey, 1986: Nonlinear interactions among internal gravity waves. *Rev. Geophys.,* **24,** 493–536.

Munk, W., 1981: Internal waves and small-scale processes. *Evolution of Physical Oceanography,* B. A. Warren and C. Wunsch, Eds., MIT Press, 264–290.

Osborn, T. R., 1980: Estimates of the local rate of vertical diffusion from dissipation measurements. *J. Phys. Oceanogr.,* **10,** 83–89.

Phillips, O. M., 1960: On the dynamics of unsteady gravity waves of finite amplitude. *J. Fluid Mech.,* **9,** 193–217.

Pinkel, R., 2008: Advection, phase distortion, and the frequency spectrum of finescale fields in the sea. *J. Phys. Oceanogr.,* **38,** 291–313.

——, and J. Smith, 1992: Repeat-sequence coding for improved precision of Doppler sonar and sodar. *J. Atmos. Oceanic Technol.,* **9,** 149–163.

Polzin, K., J. Toole, and R. Schmitt, 1995: Finescale parameterizations of turbulent dissipation. *J. Phys. Oceanogr.,* **25,** 306–328.

Rainville, L., and R. Pinkel, 2006a: Baroclinic energy flux at the Hawaiian Ridge: Observations from the R/P *FLIP. J. Phys. Oceanogr.,* **36,** 1104–1122.

——, and ——, 2006b: Propagation of low-mode internal waves through the ocean. *J. Phys. Oceanogr.,* **36,** 1220–1236.

Ruddick, B., and T. Joyce, 1979: Observations of interaction between the internal wave-field and low-frequency flows in the North Atlantic. *J. Phys. Oceanogr.,* **9,** 498–517.

Rudnick, D. L., and Coauthors, 2003: From tides to mixing along the Hawaiian Ridge. *Science,* **301,** 355–357.

Tennekes, H., and J. L. Lumley, 1972: *A First Course in Turbulence.* MIT Press, 300 pp.